Check for updates

AND-gate contrast agents for enhanced fluorescence-guided surgery

John C. Widen [1], Martina Tholen[1], Joshua J. Yim[1,2], Alexander Antaris[3], Kerriann M. Casey [4], Stephan Rogalla[5,6], Alwin Klaassen[3], Jonathan Sorger[3] and Matthew Bogyo [1,2,7] ✉

Surgical resection of tumours requires precisely locating and defining the margins between lesions and normal tissue. However, this is made difficult by irregular margin borders. Although molecularly targeted optical contrast agents can be used to define tumour margins during surgery in real time, the selectivity of the contrast agents is often limited by the target being expressed in both healthy and tumour tissues. Here, we show that AND-gate optical imaging probes that require the processing of two substrates by multiple tumour-specific enzymes produce a fluorescent signal with significantly improved specificity and sensitivity to tumour tissue. We evaluated the performance of the probes in mouse models of mammary tumours and of metastatic lung cancer, as well as during fluorescence-guided robotic surgery. Imaging probes that rely on multivariate activation to selectively target complex patterns of enzymatic activity should be useful in disease detection, treatment and monitoring.

For many cancers, surgery is the primary treatment option followed by chemotherapy and/or radiation therapy. Early detection and surgical removal of solid tumours remain the most effective way to produce a curative result. Success outcomes are highly dependent on how effectively the tumour tissue can be identified[1,2]. Accurate detection of the margin between tumour and normal healthy tissues is essential to prevent either incomplete removal of tumour cells leading to increased recurrence rates (up to 30–65% of cases)[3–5] or removal of excess healthy tissue. Furthermore, solid tumours derived from different tissues and cell types can have considerably different margin borders, making the prospects for complete removal highly variable[6]. In fact, rates of repeat surgeries for some cancer types (that is, breast cancer) are between 20% and 50% (refs. [2,7]). Thus, methods that enable both selective and sensitive real-time detection of tumour margins have the potential to positively impact surgical treatment outcomes of many of the most common types of cancer.

For most surgical treatments for cancer, imaging methods such as magnetic resonance imaging, positron emission tomography, single-photon emission computerized tomography and computerized tomography are used to diagnose and then identify the location of tumours[8]. However, these methods are not easily used intraoperatively owing to the need for large instrumentation and/or ionizing radiation. They also typically do not provide sufficient sensitivity and resolution to enable the identification of microscopic processes at the tumour margin. Alternatively, various analytical methods can be used to detect specific molecular signatures in real time during a surgical procedure. This includes the use of mass spectrometry, radio frequency, ultrasound and fluorescence lifetime detectors that enable the measurement of specific analytical signatures in the tumour microenvironment that distinguish it from the surrounding normal tissues[9–11]. However, although these types of real-time analytical devices can be highly sensitive and accurate, they are all limited by issues relating to sampling error and slow processing times

as they require the scanning of regions that are suspected to contain residual cancer.

As an alternative to using analytical detectors to scan tissues, systemically delivered optical contrast agents have the potential to broadly highlight tumour sites without any previous knowledge of tumour location[1,12]. There are presently only a small number of optical agents that are approved by the Food and Drug Administration (FDA) for use in humans and that are suitable for use with clinical camera systems. Although there has been substantial clinical benefit from dyes such as indocyanine green (ICG)[13] and 5-aminolevulinic acid[14], the main limitation is their overall non-specific mechanism of action that results in insufficient sensitivity and selectivity for use in diverse cancer types. A number of preclinical and early-stage clinical trials have begun for fluorescently tagged affinity agents, such as antibodies, peptides and small-molecule ligands[1,12,15]. There have also been advances in the development of 'smart' probes that produce a fluorescent signal only when processed by a tumour-specific enzyme (Fig. 1a). This leads to a further increase in contrast because free probe outside the tumour remains unprocessed and is not fluorescent. Proteases have become the enzymes of choice for generating smart probes because short-peptide substrates can be decorated with suitable fluorophore–quencher pairs such that probes are optically silent until they are cleaved by a protease[16–19]. Protease activity can also be used to process probes that then change their localization to be retained in cells within the tumour microenvironment[18,20]. Multiple proteases have proven to be useful biomarkers of cancerous tissues[21–24].

Previously, we designed a cysteine-cathepsin-cleavable near-infrared (NIR) substrate probe 6QC-NIR[20]. Cleavage of this substrate probe produces high signals in cancers of the lung, breast and colon, and can be detected using the FDA-approved da Vinci Si Surgical System equipped with the Firefly detection system[20]. We have found that further optimization of the reporter dye on this probe can greatly enhance its use with clinical camera systems[25].

[1]Department of Pathology, Stanford University School of Medicine, Stanford, CA, USA. [2]Department of Chemical and Systems Biology, Stanford University School of Medicine, Stanford, CA, USA. [3]Intuitive Surgical Inc., Sunnyvale, CA, USA. [4]Department of Comparative Medicine, Stanford University School of Medicine, Stanford, CA, USA. [5]Department of Medicine and Gastroenterology, Stanford University School of Medicine, Stanford, CA, USA. [6]Department of Radiology, Stanford University School of Medicine, Stanford, CA, USA. [7]Department of Microbiology and Immunology, Stanford University School of Medicine, Stanford, CA, USA. ✉e-mail: mbogyo@stanford.edu
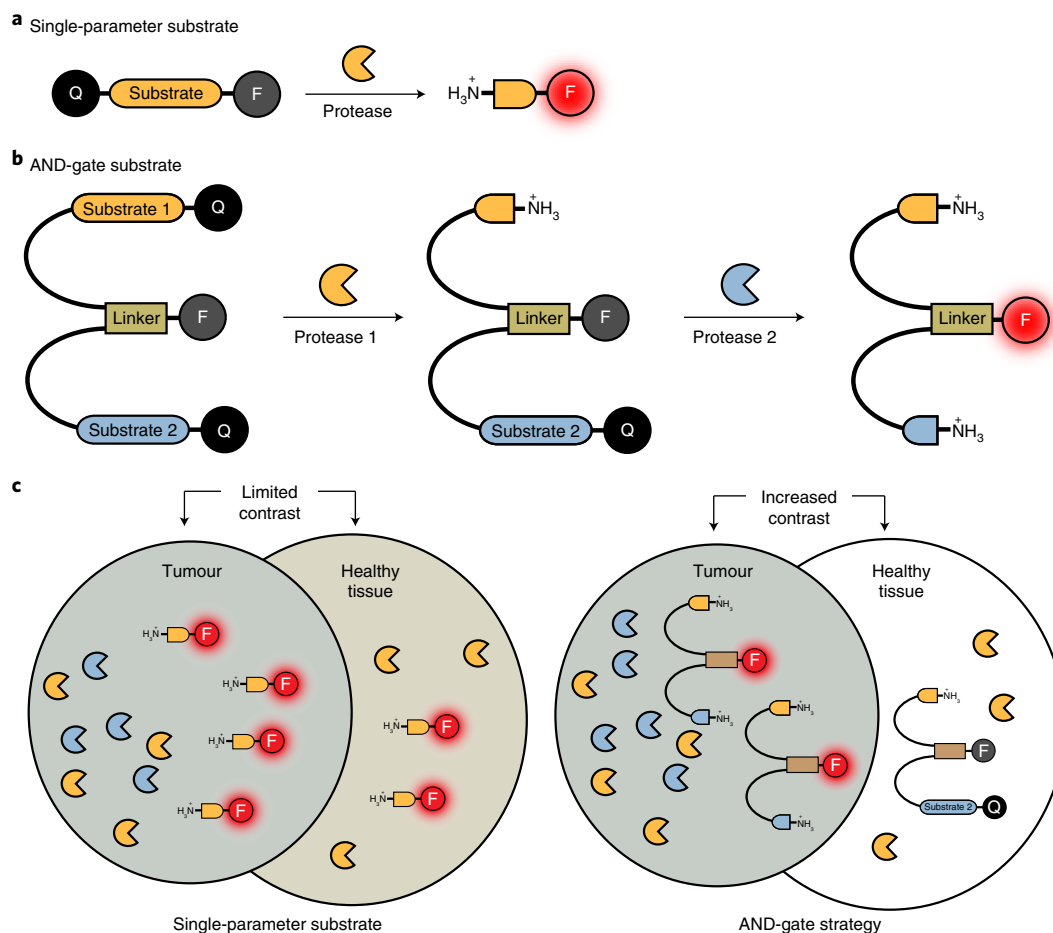
Fig. 1 | The AND-gate strategy. a, Schematic of a single-parameter quenched-fluorescent protease substrate that is cleaved by a single protease to produce a fluorescent fragment. These probes take advantage of the higher proteolytic activity in tumours to generate contrast. Q, quencher; F, fluorophore. **b**, Schematic of the multivariate AND-gate probe, which requires two proteolytic processing events to activate fluorescence. **c**, Comparison of the single-parameter and AND-gate probes in tumour and normal tissues. Higher contrast is generated by the AND-gate probe due to a lack of activation in normal tissues, which lack activity of both proteases.

However, the single greatest limitation to using protease substrates is their lack of selectivity, which results from the activity of a protease or protease family in healthy tissues as well as inside the tumour microenvironment. Here we describe a way to increase the overall tumour selectivity by designing multivariate 'AND-gate' probes in which multiple reporters must be processed within the tumour microenvironment to produce a specific optical signal (Fig. 1b,c). The term AND-gate is a Boolean logic gate that is most commonly used in computer science, but the term also represents the behaviour of molecular systems that require two orthogonal inputs to produce a single output[26]. Thus, selectivity can be greatly enhanced because the tumour is identified using multiple markers that help to distinguish it from the surrounding normal tissues. Here we demonstrate the use of the approach using probes that contain substrates for the lysosomal cysteine cathepsins that are found in tumour-associated macrophages, executioner caspases that are activated only in apoptotic cells and fibroblast activation protein α (FAP) found at invasive edges of tumours. The resulting AND-gate probes have greatly improved tumour selectivity due to the relatively high levels of apoptosis in tumours compared with surrounding normal healthy tissues and the increased activity of FAP in the tumour microenvironment. We also found that AND-gate probes have enhanced fluorescence signal within tumours compared with the corresponding cathepsin-only probe. These improved properties of the AND-gate

probes suggest that this will be a general strategy that can be used with a diverse range of enzyme substrates to increase the selectivity of optical contrast agents.

Results

Design, testing and optimization of AND-gate probes. The design of a general AND-gate strategy involves placing a fluorescent reporter into a central location such that multiple quenchers can be attached through linkages that are severed by the action of enzymes. This type of 'hub and spoke' model requires the removal of all quenchers along the spokes to liberate the central fluorescent hub. In theory, the quencher groups can be attached to the central hub using any type of enzyme-sensitive linkage, resulting in AND-gates that are responsive to a diverse array of enzyme signatures. We choose to test this design strategy using a simple glutamic acid (Glu) central linker containing a fluorescent dye that is linked to quenchers through distinct peptide sequences that could be orthogonally cleaved by two proteases with non-overlapping substrate specificities. The central Glu linker is ideal because a sulfo-Cy5 fluorophore can be attached to its free α-amine and each peptide substrate containing a sulfo-QSY21 quencher can be connected through amide bonds to the remaining carboxylic acids (Fig. 2a). This positions the quenchers such that fluorescence activation occurs only after both peptides have been cleaved. Furthermore, by using diamino-alkyl

linkers between the peptides and the Glu core, the final fluorescent fragment will contain two free amine groups that induce lysosomal accumulation of the probe, as we have demonstrated for our cathepsin substrate probes[20].

We chose peptide substrates that have previously been shown to be specifically processed by caspase 3 (Casp3; DEVDGP)[27] and the cysteine cathepsins (z-FK)[28]. These sequences were optimal for the first-generation AND-gate probe because Casp3 and cathepsins have highly orthogonal substrate specificities and, therefore, each protease can process only its corresponding substrate. Although these substrate sequences are selective for the protease or class of proteases, non-specific activation still occurs in vivo for all single-substrate probes to some extent. The AND-gate strategy diminishes this non-specific activation by requiring that both processing events are present at the same location. A subset of cathepsins are upregulated in tumour-associated macrophages[29–31] and present in most normal tissues, whereas Casp3 activity is increased in tumours but is generally not active in healthy cells, except during development[32]. As Casp3 activity occurs in the cytosol of apoptotic cells with compromised cell membranes, probes targeting this protease require a mechanism to induce accumulation[33,34]. We expected that processing by cathepsins coupled with Casp3 would induce lysosomal accumulation of the processed AND-gate probe. Furthermore, both proteases are active within tumours but are not expected to be active together in healthy tissues, making them ideal targets for our AND-gate probe strategy.

We synthesized a first-generation AND-gate probe, DEATH-CAT-1, containing the natural L-Glu central linker (Fig. 2a and Supplementary Scheme 1). We also synthesized negative controls in which a D-Asp (D-aspartic acid) was used in place of the natural L-Asp in the P1 position of the Casp3 sequence (D-Asp-1) and a D-Phe (D-phenylalanine) was used in the P2 position of the CAT sequence (D-Phe-1). To test the DEATH-CAT-1 probe, we incubated it with recombinant human CATL, CATB, CATS or Casp3 either separately or sequentially in combinations (Supplementary Fig. 1a,b). Importantly, we found that the probe produced a fluorescence signal only when both cathepsin and Casp3 were incubated sequentially. We also found that both control probes remained non-fluorescent after incubation with both proteases, regardless of the order of addition, therefore validating the overall concept of the AND-gate strategy (Supplementary Fig. 1c,d). We next tested the stability of the linker using total tissue lysates derived from homogenized 4T1 breast tumours (Supplementary Fig. 1e). As expected, we found that the DEATH-CAT-1 probe was activated and the D-Asp-1 negative control remained non-fluorescent. However, the D-Phe-1 probe was activated in the 4T1 lysate. As the D-Phe-1 probe was not

cleaved by the purified cathepsins, the results from the lysate suggest that it is probably cleaved by hydrolysis of the glutamine amide in the linker by other enzymes to release the CAT sequence (z-FK) and produce the observed fluorescence signal.

Given the instability at the glutamine α-acid, we synthesized a second-generation probe, DEATH-CAT-2, and the respective negative controls D-Phe-2 and D-Asp-2, in which the natural L-Glu was replaced by the unnatural D-Glu (Fig. 2a and Supplementary Scheme 2). We evaluated this second-generation set of probes using an in vitro fluorogenic assay with recombinant proteases and found that the probes performed similarly to the first-generation probes with only DEATH-CAT-2 producing signal, and only after adding both CATL and Casp3 (Fig. 2b,c). Using liquid chromatography coupled with mass spectrometry analysis, we detected the expected cleavage products after incubation with CATL or Casp3 alone, and with both proteases successively (Supplementary Fig. 2). Importantly, the second-generation negative control probes containing the D-Glu linker showed good stability in tumour lysates; both remained inactive even after 2 h of incubation (Fig. 2d). Interestingly, DEATH-CAT-2 was activated at a faster rate and with an overall higher signal compared with 6QC in tumour lysate. DEATH-CAT-2 was also selective for Casp3 over other related initiator and executioner caspases (Supplementary Fig. 3).
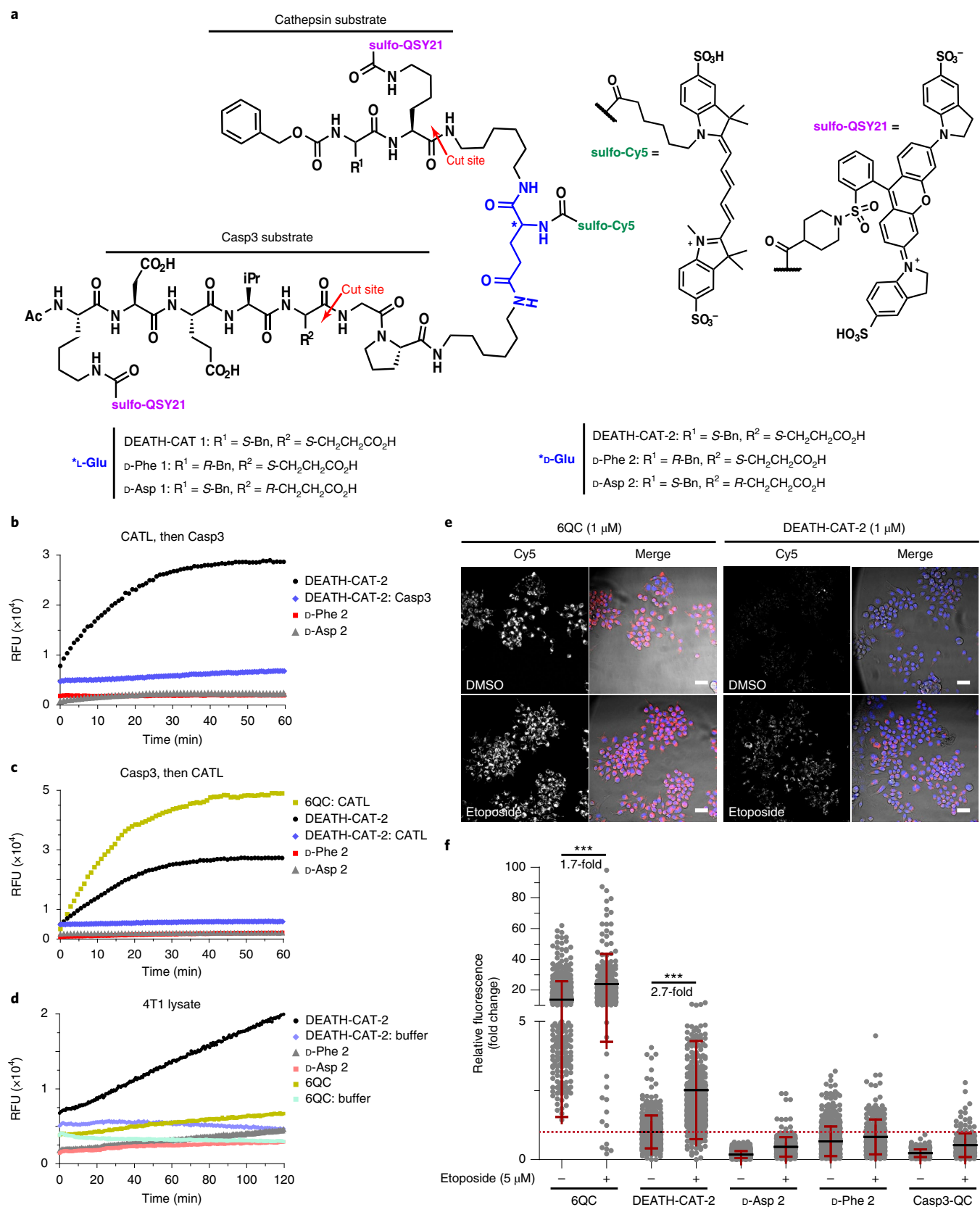
Having solved the issue of linker stability, we tested the specificity of activation of the DEATH-CAT-2 probe using a coculture of breast tumour 4T1 cells and RAW macrophages. Cells were first incubated with dimethyl sulfoxide (DMSO) or the cytotoxic agent etoposide (5 μM) for 24 h to induce apoptosis. The 6QC, DEATH-CAT-2, Casp3-QC (single-substrate probe for Casp3; Supplementary Fig. 4) and respective negative control probes were added to the cells for 2 h before acquiring images (Fig. 2e and Supplementary Fig. 5). Sufficient fluorescence activation of DEATH-CAT-2 compared with the background was achieved within 2 h. At later time points, a large portion of cells had died, which reduces the number of adherent cells for imaging. As expected, none of the negative control probes were activated under either condition; by contrast, 6QC was activated independently of apoptosis induction, and DEATH-CAT-2 was activated only in the apoptotic cells (Fig. 2e,f). These results confirm that the DEATH-CAT-2 probe requires processing by both proteases to produce a fluorescent product that accumulates inside macrophage lysosomes.

AND-gate probes improve tumour selectivity in vivo. We next evaluated the DEATH-CAT-2 probe and its respective negative controls in a 4T1 mouse model of breast cancer. We chose this model because it enables direct imaging of live animals using a
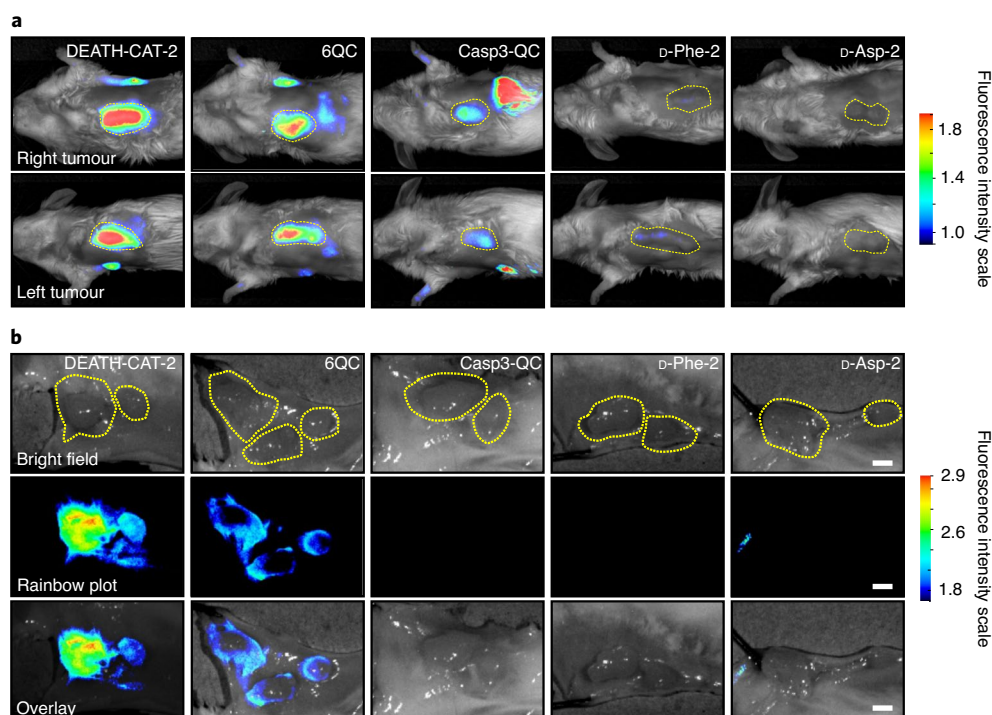
Fig. 2 | Structure and in vitro validation of AND-gate probes. a, Structures of the dual orthogonal protease substrate AND-gate probes and the corresponding negative controls. DEATH-CAT-1 contains the natural amino acid L-Glu, whereas DEATH-CAT-2 contains an unnatural D-Glu linker (blue). The negative control probes contain either a D-Asp in the P1 position of the Casp3 sequence (D-Asp-1) or D-Phe in the P2 position of the CAT sequence (D-Phe-1) to block proteolytic cleavage by the respective protease. **b**, Progress curve of DEATH-CAT-2 incubated with CATL followed by Casp3 compared with negative control probes D-Phe-2 and D-Asp-2 and with Casp3 only (10 nM). All substrates were used at 10 μM. RFU, relative fluorescence units. **c**, Progress curves as described in **b** except that Casp3 was added first followed by addition of CATL. The single-substrate probe 6QC was incubated with CATL alone. **d**, Progress curve over 2 h incubation of DEATH-CAT-2 compared with 6QC and the corresponding negative controls, D-Phe-2 and D-Asp-2, in either buffer or tumour lysate generated from 4T1 breast tumours in BALB/c mice. **e**, Representative fluorescence microscopy images of 4T1 cells cocultured with RAW macrophages (1:1 ratio) labelled with either the single-parameter cathepsin probe 6QC or the DEATH-CAT-2 probe. Cells were incubated with either DMSO or etoposide (5 μM) for 24 h before adding probes (1 μM). After 2 h, Hoechst stain was added to visualize nuclei and the cells were imaged. The Cy5 signal is shown in greyscale (left). For merged images on the right, the bright-field image (greyscale), nuclear staining (blue) and Cy5 probe signal (red) are shown. Representative images of the negative controls D-Phe-2, D-Asp-2 and Casp3-QC are provided in the Supplementary Information. Scale bars, 20 μm. **f**, Quantification of the fluorescence signal from the experiments in **e** shown as the fold change in corrected total cellular fluorescence normalized to cells incubated with DMSO and the DEATH-CAT-2 probe. Red dotted line indicates averaged background fluorescence level of DEATH-CAT 2 in DMSO control. Statistical analysis was performed using two-tailed Mann–Whitney U-tests; ***$P < 0.0001$. Sample mean ± s.d., sample size (n): 6QC (DMSO), 13.6 ± 12.1, $n = 416$; 6QC (etoposide), 23.9 ± 19.6, $n = 266$; DEATH-CAT-2 (DMSO), 1.0 ± 0.6, $n = 398$; DEATH-CAT-2 (etoposide), 2.7 ± 1.8, $n = 462$; D-Asp-2 (DMSO), 0.7 ± 0.5, $n = 599$; D-Asp-2 (etoposide), 0.8 ± 0.6, $n = 246$; D-Phe-2 (DMSO), 0.2 ± 0.1, $n = 402$; D-Phe-2 (etoposide): 0.5 ± 0.4, $n = 269$; Casp3-QC (DMSO), 0.2 ± 0.1, $n = 226$; Casp3-QC (etoposide), 0.5 ± 0.4, $n = 205$. Data were acquired from three biological replicates. The total images taken for each condition included three fields of view per well from six separate wells.

NIR imaging system. The tumour-specific signal can be measured relative to surrounding background tissues and tissues can be subsequently removed for quantifying and determining the overall probe activation in major organs distant to the tumour site.

We imaged live animals 2 h after injection of probes and found that the DEATH-CAT-2 probe showed strong tumour accumulation that resulted in a brighter tumour signal compared with the cathepsin-only substrate 6QC and the Casp3-only substrate probe

a

Cathepsin substrate

sulfo-QSY21

Cut site

sulfo-Cy5 =

sulfo-QSY21 =

Casp3 substrate

Cut site

sulfo-Cy5

sulfo-QSY21

*L-Glu

DEATH-CAT 1: $R^1 = S$-Bn, $R^2 = S$-CH$_2$CH$_2$CO$_2$H
D-Phe 1: $R^1 = R$-Bn, $R^2 = S$-CH$_2$CH$_2$CO$_2$H
D-Asp 1: $R^1 = S$-Bn, $R^2 = R$-CH$_2$CH$_2$CO$_2$H

*D-Glu

DEATH-CAT-2: $R^1 = S$-Bn, $R^2 = S$-CH$_2$CH$_2$CO$_2$H
D-Phe 2: $R^1 = R$-Bn, $R^2 = S$-CH$_2$CH$_2$CO$_2$H
D-Asp 2: $R^1 = S$-Bn, $R^2 = R$-CH$_2$CH$_2$CO$_2$H

b CATL, then Casp3

- DEATH-CAT-2
- DEATH-CAT-2: Casp3
- D-Phe 2
- D-Asp 2

c Casp3, then CATL

- 6QC: CATL
- DEATH-CAT-2
- DEATH-CAT-2: CATL
- D-Phe 2
- D-Asp 2

d 4T1 lysate

- DEATH-CAT-2
- DEATH-CAT-2: buffer
- D-Phe 2
- D-Asp 2
- 6QC
- 6QC: buffer

e

6QC (1 µM)   DEATH-CAT-2 (1 µM)

Cy5   Merge   Cy5   Merge

DMSO

Etoposide

f

Etoposide (5 µM)

6QC   DEATH-CAT-2   D-Asp 2   D-Phe 2   Casp3-QC

Fig. 3 | Enhanced selectivity and sensitivity of DEATH-CAT-2 in the 4T1 breast tumour model. a, Images of live mice bearing 4T1 breast tumours 2 h after probe injection (20 nmol, i.v.). **b**, Representative images of splayed 4T1 tumours 2 h after injection. The fluorescence signals in tumours in live and splayed mice are shown as rainbow plots and are normalized across representative images from each cohort. Fluorescence intensity scales on the right are arbitrary RFU. Outlines of the tumours are shown (yellow dotted lines). Scale bars, 3 mm. The representative images presented were acquired from at least ten biological replicates. All of the images of live mice bearing 4T1 breast tumours from this study are provided in the Supplementary Information.

Casp3-QC (Fig. 3a). Importantly, the negative control probes produced no visible signals, confirming the linker stability observed in vitro. Mice were splayed to show localized fluorescence signal within the tumours compared with surrounding fat tissue (Fig. 3b). Quantification of average tumour fluorescence in splayed tumours confirmed that both the DEATH-CAT-2 and single-substrate probe 6QC produced a significantly increased signal compared with the negative controls D-Phe-2 and D-Asp-2, and that the level of contrast over controls was several-fold higher for the AND-gate probe (Fig. 4a). The Casp3-specific substrate probe Casp3-QC, which has only the caspase half of the AND-gate substrate, showed low-level tumour signal; however, it was not significantly higher than the two negative control probes. The tumour-to-background ratio (TBR) of DEATH-CAT-2 was also significantly increased compared with the single-parameter 6QC probe (mean ± s.d., 3.0 ± 0.3 compared with 2.3 ± 0.5; Supplementary Fig. 6).

To determine the fluorescence activation in healthy organs compared with in tumours, we excised relevant organs for ex vivo imaging and quantified the fluorescence signal intensities. We found that the fluorescence signals in excised liver, kidney and lung tissue was significantly reduced in the animals treated with DEATH-CAT-2 compared with those treated with 6QC (Fig. 4c). Quantification of the fold change in fluorescence signals over tumour signals for each tissue confirmed the substantial increase in selectivity of the AND-gate probe compared with the cathepsin-only 6QC probe (Fig. 4d). As a further analysis of probe activation in vivo, we fixed and embedded excised tumours for cryosectioning and immunofluorescence analysis (Fig. 4b). We stained tumour sections for CD68, a marker of macrophages, as well as for cleaved Casp3. This analysis confirmed the presence of macrophages within the 4T1 breast tumours, as has been previously described[20]. We also observed numerous regions within the tumour tissues in which

cells contained active Casp3. These regions of apoptotic cells were always found directly adjacent to, or colocalized with, macrophage cell populations. The brightest probe signal was always found at the intersection between macrophages and cells with active Casp3 confirming that Casp3 and cathepsins are both active within a tumour and generally found in close proximity making them ideal targets for use in the AND-gate strategy.

Application to fluorescence-guided surgery. To evaluate the performance of our AND-gate probe strategy during robotic fluorescence-guided surgery, we synthesized an AND-gate probe containing a fluorophore that has excitation and emission wavelengths that are compatible with the FDA-approved Firefly detection system on the da Vinci Xi Surgical System. At present, the Firefly fluorescence detection system is specifically tuned to the excitation/emission properties of ICG (ex/em, 780/820 nm). We initially sought to synthesize an AND-gate probe containing the conjugatable version of ICG (containing a carboxylic acid) and the respective quencher QC-1, which is non-fluorescent and has strong absorbance between 600–900 nm. However, conjugating ICG to the peptide scaffold caused unexpected issues that were possibly caused by aggregation or tertiary folding of the molecule. We therefore used a heptamethine cyanine fluorophore FNIR tag that was designed to resist aggregation and have better water solubility compared with ICG[35]. We conjugated the FNIR dye successfully to the α-amine on the central D-Glu linker and subsequently attached two QC-1 quenchers to the lysine side chains to produce DEATH-CAT–FNIR (Supplementary Scheme 3). Although this fluorophore has slightly lower excitation/emission maximum wavelengths compared with ICG (ex/em, 765/788 nm), the fluorescence can be detected using the Firefly detection system, albeit with lower sensitivity compared with ICG. We confirmed that DEATH-CAT–FNIR was efficiently
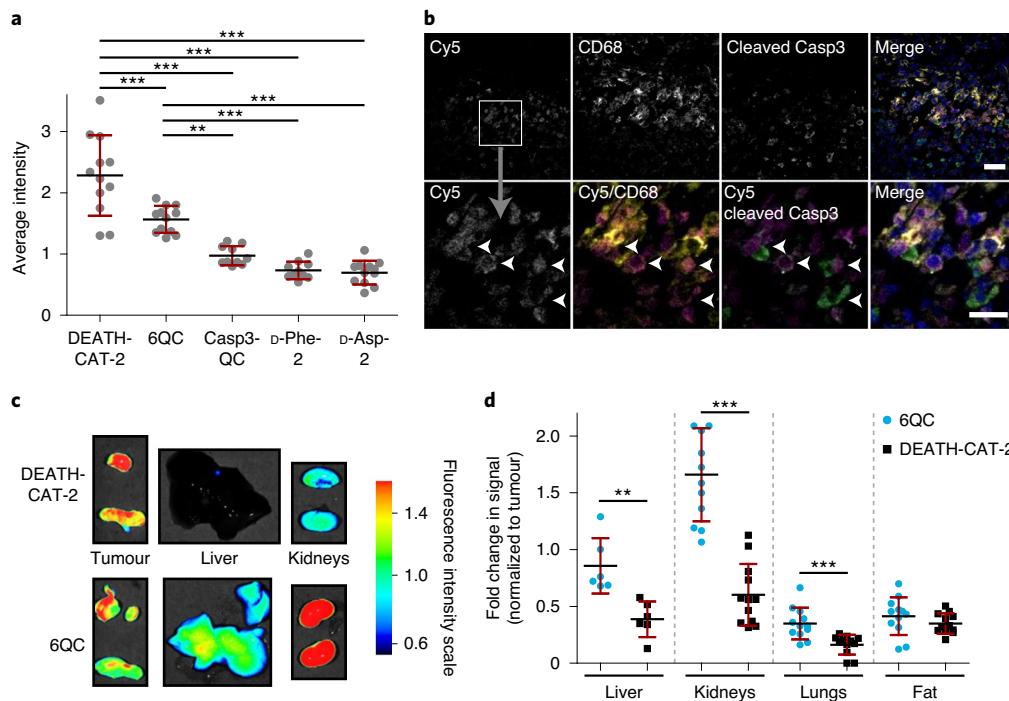
Fig. 4 | Quantitative analysis of DEATH-CAT-2 compared with single substrates and negative controls in the 4T1 breast tumour model. a, The average fluorescence signal within splayed tumours from all mice 2 h after injection of each probe (20 nmol, i.v.). Statistical analysis was performed using one-way analysis of variance (ANOVA) with Tukey's multiple comparison test; multiplicity-adjusted P values, $**P = 0.002$, $***P < 0.0001$. Sample mean $\pm$ s.d., sample size (n): DEATH-CAT-2, 2.3 $\pm$ 0.7, $n = 12$; 6QC, 1.6 $\pm$ 0.2, $n = 12$; Casp3-QC, 1.0 $\pm$ 0.2, $n = 10$; D-Phe-2, 0.7 $\pm$ 0.1, $n = 10$; D-Asp-2, 0.7 $\pm$ 0.2, $n = 12$. **b**, Immunofluorescence microscopy images of 4T1 tumour sections from mice treated with DEATH-CAT-2 and stained for cleaved Casp3 and CD68 using specific antibodies. Single-channel images are in greyscale. The merged images show Cy5 (probe; magenta), CD68 (yellow), cleaved Casp3 (green) and DAPI (blue). White arrows indicate probe-positive macrophages that are proximal to cells positive for cleaved Casp3. The same contrast and brightness settings were used to process each image. Scale bars, 50 μm (top row), 10 μm (bottom row). Images of additional examples of stained 4T1 tumour sections are provided in the Supplementary Information and are representative of 50 fields of view. **c**, Images of excised organs of mice (2 h after injection). Fluorescence signal is shown as rainbow plots and is normalized between images. Fluorescence intensity scale on the right is arbitrary RFU. Images are representative of each cohort. **d**, The fold change in fluorescence signal compared with tumour signals for each tissue type in mice treated with the indicated probes. Statistical analysis was performed using two-tailed Student's t-tests with the Bonferroni–Holm procedure; unadjusted P values, $**P = 0.01$, $***P < 0.001$. Sample mean $\pm$ s.d., sample size (n): 6QC (liver), 0.9 $\pm$ 0.2, $n = 6$; DEATH-CAT-2 (liver), 0.4 $\pm$ 0.2, $n = 6$; 6QC (kidneys), 1.7 $\pm$ 0.4, $n = 12$; DEATH-CAT-2 (kidneys), 0.6 $\pm$ 0.3, $n = 12$; 6QC (lungs), 0.3 $\pm$ 0.1, $n = 12$; DEATH-CAT-2 (lungs), 0.2 $\pm$ 0.1, $n = 12$; 6QC (fat), 0.4 $\pm$ 0.2, $n = 12$; DEATH-CAT-2 (fat), 0.3 $\pm$ 0.1, $n = 12$. Overlay images of fluorescence signal and bright-field images of all live mice, splayed tumours and excised organs from each cohort are provided in the Supplementary Information. The data presented were acquired from at least ten biological replicates.

processed by CATL and Casp3 using the recombinant proteases in a fluorogenic substrate assay (Supplementary Fig. 10). Similar to the Cy5 AND-gate probes, DEATH-CAT–FNIR produced a fluorescence signal only after incubation with both proteases, regardless of the order of addition.

We evaluated the performance of DEATH-CAT–FNIR with the single-substrate probes 6QC-ICG and 6QC-NIR as positive controls during robotic surgery on mice bearing 4T1 breast tumours. Both single-substrate probes were developed in our laboratory and contain either an ICG or DyLight 780-B1 (NIR) fluorophore, which are activated by cysteine cathepsin proteases[25]. We injected mice bearing 4T1 breast tumours with probes 2 h before performing robotic surgery (20 nmol, intravenously (i.v.)). DEATH-CAT–FNIR produced fluorescence contrast in the tumour compared with the surrounding tissue, which clearly highlighted the margins during surgery (Fig. 5a). Despite using a fluorophore with lower excitation/emission wavelengths compared with ICG, DEATH-CAT–FNIR had comparable fluorescence signal intensity to the 6QC-ICG probe and much improved signal in comparison to 6QC-NIR, which also has lower excitation/emission wavelengths than ICG (ex/em, 788/799 nm).

To further demonstrate the utility of the DEATH-CAT–FNIR probe, we performed a resection of a primary subcutaneous

mammary tumour and subsequently used probe fluorescence to assess the remaining subcutaneous tumour bed (Fig. 5b). The residual cancer cells that were remaining after excising the primary tumour were not visible using white-light imaging but could be easily visualized using Firefly detection of the probe signal (Supplementary Video 1). We next removed the subcutaneous tumour bed and overlying skin with surrounding probe-negative tissue. This tissue was formalin-fixed and sectioned such that haematoxylin and eosin (H&E) slides contained both probe-positive and probe-negative regions on a single slice. Analysis of the H&E-stained tissues by a board-certified pathologist confirmed that the regions showing probe activation contained residual tumour left behind after excision, whereas probe-negative regions contained normal subcutaneous and cutaneous tissue (Fig. 5c,d). Thus, the DEATH-CAT–FNIR probe was able to accurately detect areas of residual tumour cells that remained after excision of a bulk tumour.

After robotic surgery, tumours and organs from mice injected with each probe were imaged ex vivo using the LiCor Pearl imaging system to quantify the fluorescence signal. Representative images of excised tumours and organs confirmed a reduced signal in the liver and kidneys compared with the signal found in the tumours for DEATH-CAT–FNIR, whereas both of the 6QC probes showed
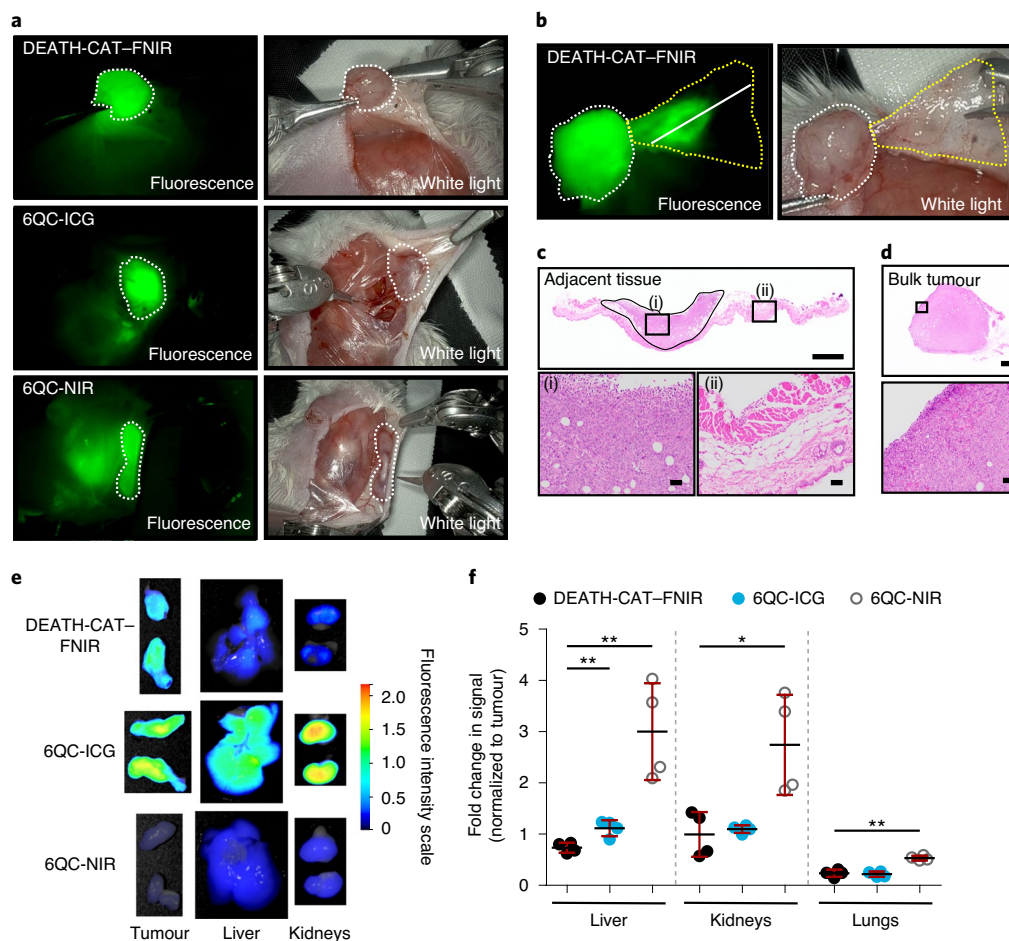
Fig. 5 | Images from robotic fluorescence-guided surgery and quantification of fluorescence signal in healthy organs. a, Screen captures of the fluorescence signal and bright-field views during dissection of 4T1 breast tumours in mice injected with DEATH-CAT–FNIR, 6QC-ICG or 6QC-NIR (20 nmol, i.v.). Tumours are indicated (white dotted line). **b**, Screen-capture images (fluorescence and white light) of a primary excised tumour (white dotted line) and the resulting adjacent tissue (yellow dotted line). The remaining tumour bed (including the subcutaneous and cutaneous tissue) was excised for sectioning. Histological analysis was performed on sections of the tumour bed (the solid white line indicates the position of the histological section) and the bulk tumour. Sectioning was performed perpendicular to the plane of the image. **c**, H&E staining of the adjacent probe-positive and probe-negative tissue; regions of residual tumour (i) and the surrounding healthy tissue (ii) are indicated. The black outline indicates area of the tumour within the section. Images are representative of ten stepwise sections through the tissue. Scale bars, 500 µm (top), 50 µm (bottom). **d**, H&E staining of a section taken from the bulk tumour; a magnification of the area indicated by the black box is shown at the bottom. Scale bars, 500 µm (top), 50 µm (bottom). **e**, Representative images of excised tumours and healthy organs. Fluorescence intensity scale on the right is arbitrary RFU. Signals are normalized and displayed as rainbow plots overlaid on bright-field images. **f**, Relative quantification of fluorescence signal in liver, kidneys and lungs normalized to tumour signal. Statistical analysis was performed using two-tailed Student's t-tests; $*P = 0.017$ (kidney, DEATH-CAT–FNIR versus 6QC-NIR), $**P = 0.003$ (liver, DEATH-CAT–FNIR versus 6QC-NIR), $**P = 0.006$ (liver, DEATH-CAT–FNIR versus 6QC-ICG), $**P < 0.001$ (lung, DEATH-CAT–FNIR versus 6QC-NIR). Sample mean ± s.d., sample size (n): DEATH-CAT–FNIR (liver), 0.7 ± 0.1, $n = 4$; 6QC-ICG (liver), 1.1 ± 0.2, $n = 4$; 6QC-NIR (liver), 3.0 ± 0.9, $n = 4$; DEATH-CAT–FNIR (kidneys), 1.0 ± 0.4, $n = 4$; 6QC-ICG (kidneys), 1.1 ± 0.7, $n = 4$; 6QC-NIR (kidneys), 2.7 ± 1.0, $n = 4$; DEATH-CAT–FNIR (lungs), 0.2 ± 0.1, $n = 4$; 6QC-ICG (lungs), 0.2 ± 0.1, $n = 4$; 6QC-NIR (lungs), 0.5 ± 0.0, $n = 4$. The data presented were acquired from four biological replicates.

high background outside of the tumours (Fig. 5e). Quantification of the signal in healthy organs normalized to the tumour signal confirmed a significant reduction in background in the liver for mice injected with DEATH-CAT–FNIR compared with both 6QC probes and a significant reduction in background for all healthy organs compared with 6QC-NIR (Fig. 5f).

AND-gate probe targeting FAPα and cathepsins. To demonstrate the generality of the AND-gate approach for the development of targeted quenched-fluorescent probes, we sought to combine the successful CAT substrate sequence (z-FK) with another protease that is highly expressed in the tumour microenvironment. We chose FAP because it has increased proteolytic activity in a broad range of

tumour types and has a unique substrate specificity profile with a strong preference for a Gly-Pro (GP) sequence[36,37]. We synthesized and evaluated three single-substrate FAP probes containing a GP, Gly-Pro-Asn (GPN) and Gly-Pro-Ser (GPS) amino acid sequence to validate and further optimize a FAP sequence for incorporation into an AND-gate probe (Supplementary Fig. 11a). Adding an additional P1′ asparagine or serine has been demonstrated to increase specificity for FAP and increase the rate of substrate turnover[38–40]. The GPN and GPS sequences containing a sulfo-Cy5/sulfoQSY-21 had an approximately twentyfold increase in initial velocities compared with the GP sequence (Supplementary Fig. 11b). We chose the GPS sequence for incorporation into an AND-gate probe to increase the solubility of the probe. Attempts to synthesize an
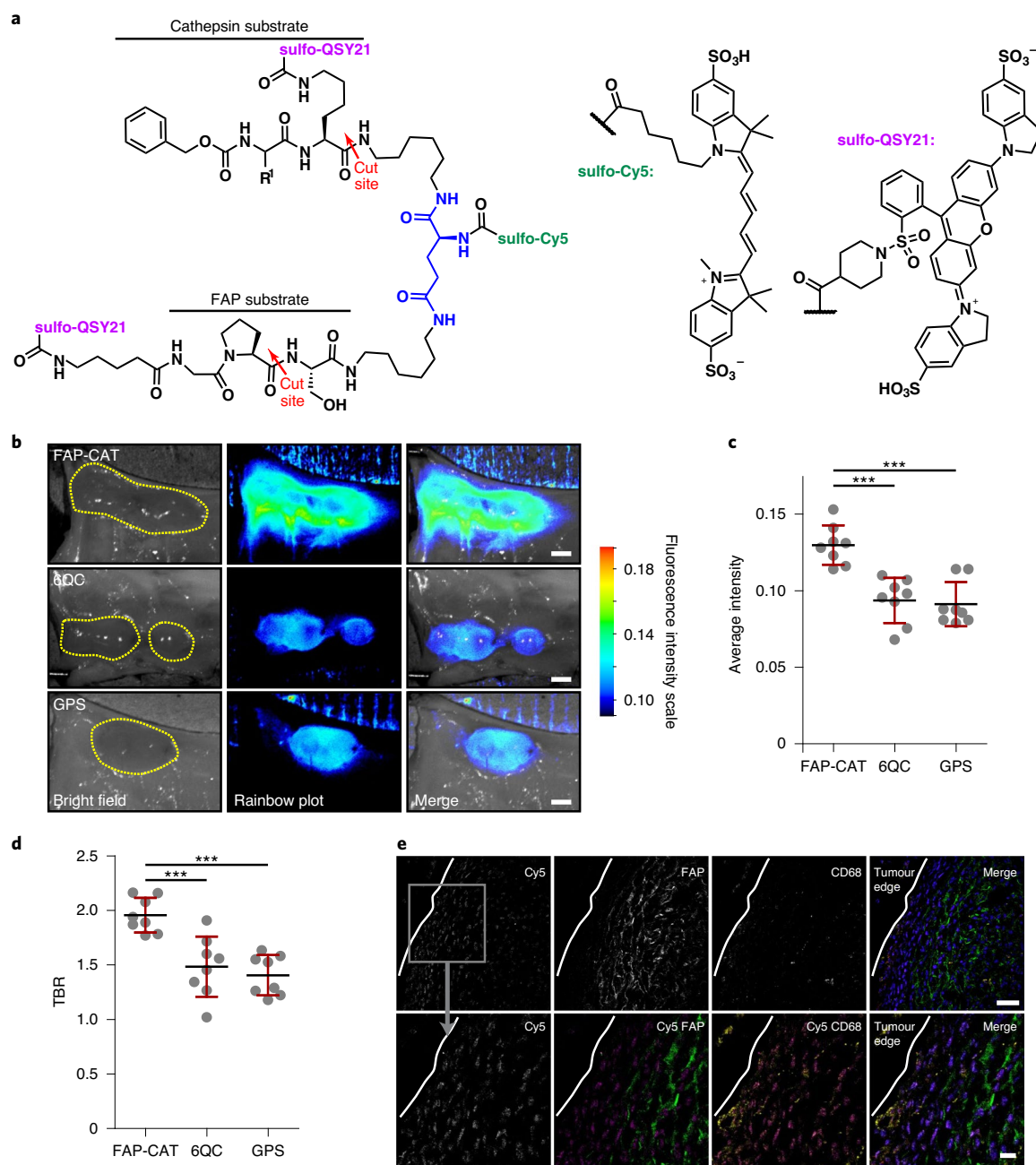
Fig. 6 | Structure of the FAP-CAT AND-gate probe and evaluation in a 4T1 breast tumour model. a, Structure of the FAP-CAT AND-gate probe.
b, Representative bright-field, rainbow plot and overlay images of splayed 4T1 tumours 4 h after tail-vein injection of FAP-CAT, 6QC and GPS (20 nmol). Fluorescence intensity scale on the right is arbitrary RFU. The yellow dotted lines indicate the tumours in the bright-field images. Scale bars, 3 mm. **c**, The average fluorescence intensity of splayed tumours from each cohort. Statistical analysis was performed using one-way ANOVA and a two-tailed Student's t-test; ***$P < 0.0001$. Rainbow plots overlaid on bright-field images of all mice, representative of eight images from each cohort, are provided in the Supplementary Information. Sample mean ± s.d., sample size (n): FAP-CAT, 0.13 ± 0.01, $n = 8$; 6QC, 0.9 ± 0.1, $n = 8$; GPS, 0.9 ± 0.1, $n = 8$. **d**, The TBR of splayed tumours from each mouse cohort receiving probe. Statistical analysis was performed using one-way ANOVA and a two-tailed Student's t-test; ***$P < 0.001$. Sample mean ± s.d., sample size (n): FAP-CAT, 2.0 ± 0.2, $n = 8$; 6QC, 1.5 ± 0.3, $n = 8$; GPS, 1.4 ± 0.2, $n = 8$. **e**, Immunofluorescence microscopy images of the edge of a 4T1 tumour dissected from a mouse injected with the FAP-CAT probe. Scale bars, 50 μm (top), 10 μm (bottom). The white line indicates the edge of the tumour. Single-channel images are shown in greyscale. The merged images show Cy5 (probe; magenta), CD68 (yellow), FAP (green) and DAPI (blue). The same contrast and brightness settings were used to process each image. Images of additional examples of stained 4T1 tumour sections are provided in the Supplementary Information and are representative of 30 fields of view. The data presented were acquired from four biological replicates.

AND-gate probe using the GPN sequence caused issues during the synthesis.

We synthesized an AND-gate probe containing the cathepsin and FAP sequences, FAP-CAT, using the same chemistry and linker used for the DEATH-CAT probe (Supplementary Scheme 4). The structure of the FAP-CAT probe is shown in Fig. 6a and contains a central D-Glu linker and a sulfo-Cy5/sulfo-QSY21 fluorophore–quencher system. We confirmed that the FAP-CAT probe activates
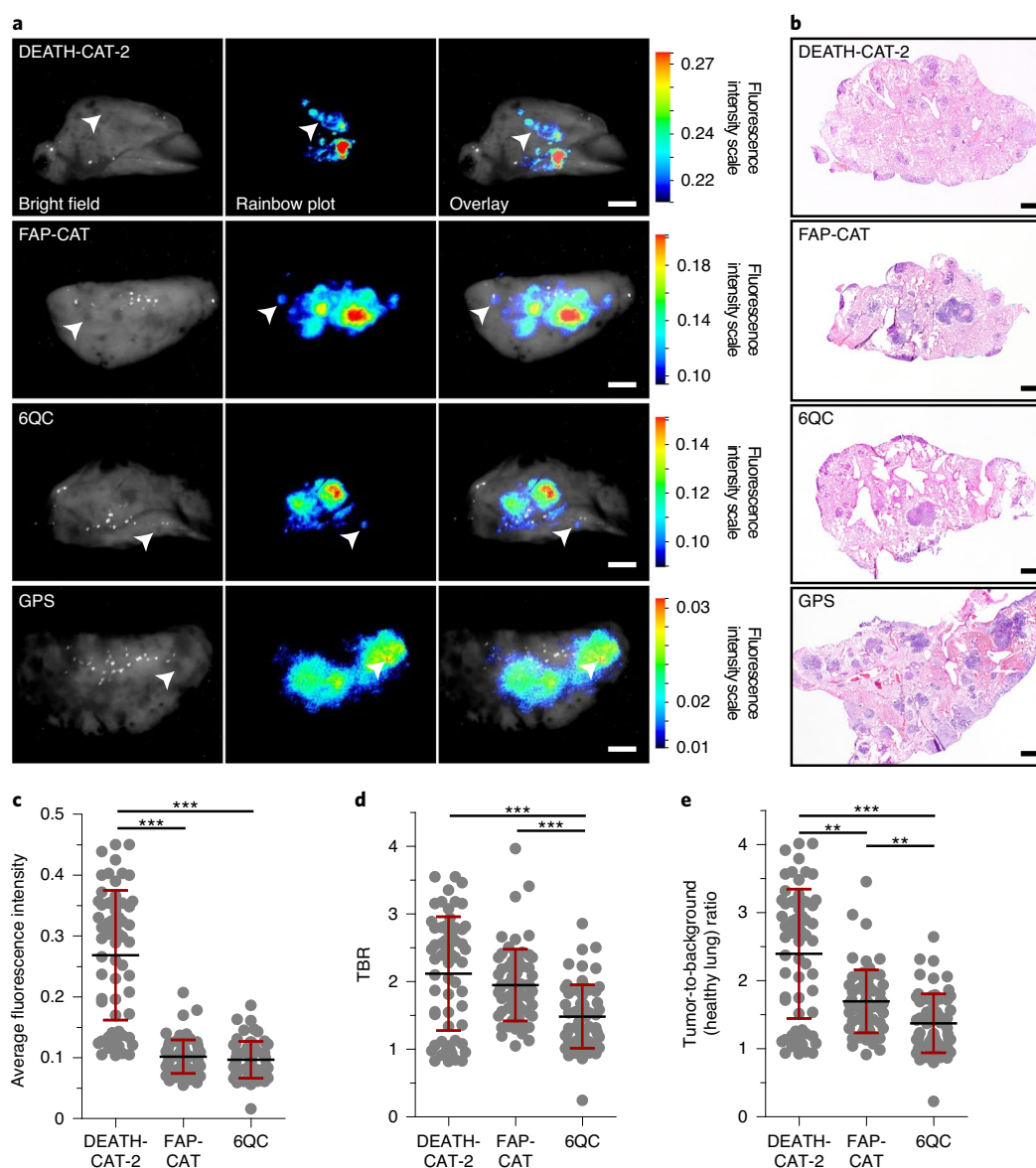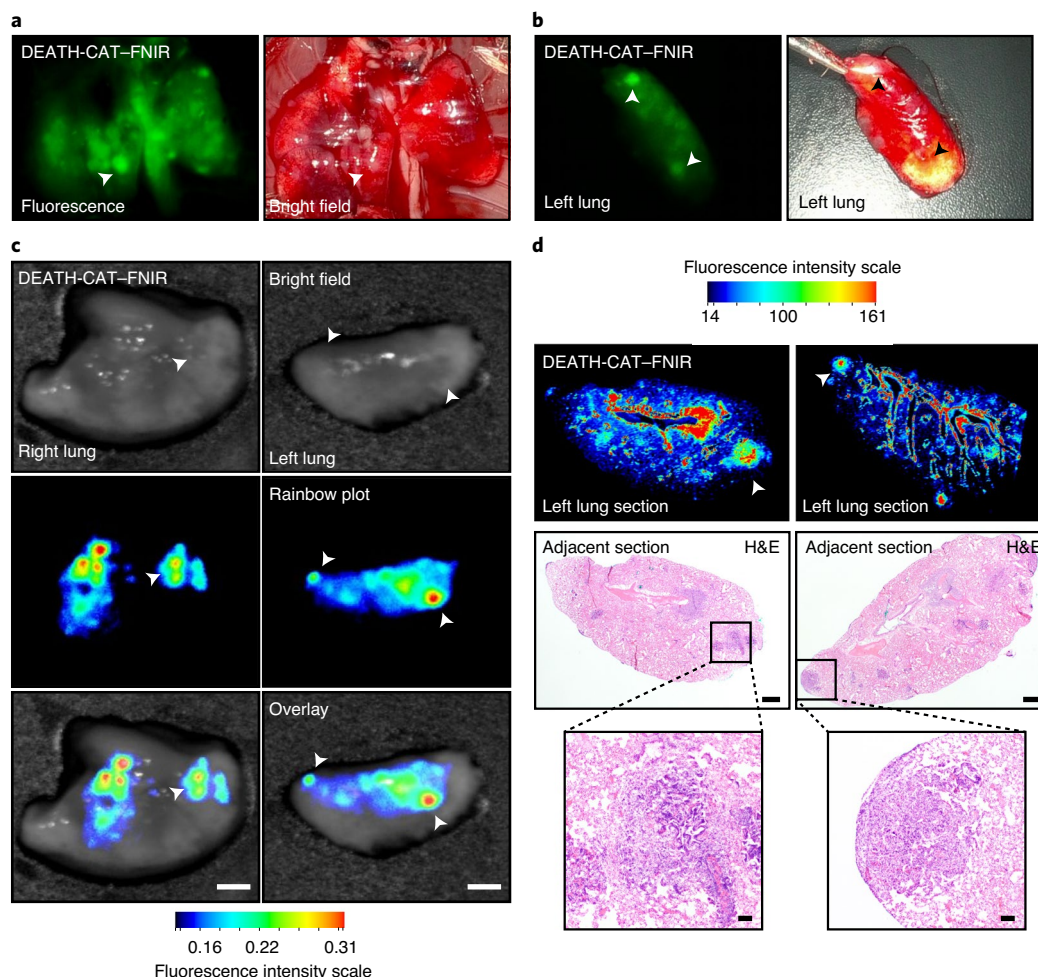
Fig. 7 | Evaluation of AND-gate probes in a mouse model of lung metastasis. a, Representative bright-field, rainbow plot and overlay images of resected lungs bearing metastases 16 h after tail-vein injection of DEATH-CAT-2, FAP-CAT, 6QC and GPS (30 nmol). Fluorescence intensity scales on the right are arbitrary RFU. The white arrows indicate example metastases. Scale bars, 3 mm. Four total images were taken for each cohort. **b**, Representative H&E staining of sections from imaged lungs bearing metastases. Scale bars, 1 mm. Images are representative of five sections stepwise through each tissue. **c**, The average fluorescence intensity within identified lung tumour nodules. Statistical analysis was performed using the Kruskal–Wallis test with Dunn's multiple comparison test; multiplicity-adjusted P value, ***$P < 0.0001$. Sample mean ± s.d., sample size (n): DEATH-CAT-2, 0.27 ± 0.11, $n = 63$; FAP-CAT, 0.10 ± 0.03, $n = 66$; 6QC, 0.10 ± 0.03, $n = 65$. **d**, The TBR for tumours was calculated using adjacent lung tissue. Statistical analysis was performed using the Kruskal–Wallis test with Dunn's multiple comparison test; multiplicity-adjusted P value, ***$P < 0.0001$. Sample mean ± s.d., sample size (n): DEATH-CAT-2, 2.1 ± 0.8, $n = 63$; FAP-CAT, 2.0 ± 0.5, $n = 66$; 6QC, 1.5 ± 0.5, $n = 65$. **e**, The TBR was calculated using signals from healthy mouse lungs without tumours. Statistical analysis was performed using the Kruskal–Wallis test with Dunn's multiple comparison test; multiplicity-adjusted P values: **$P = 0.004$ (DEATH-CAT-2 versus FAP-CAT), **$P = 0.003$ (FAP-CAT versus 6QC), ***$P < 0.0001$ (DEATH-CAT-2 versus 6QC). Sample mean ± s.d., sample size (n): DEATH-CAT-2, 2.4 ± 1.0, $n = 63$; FAP-CAT, 1.7 ± 0.5, $n = 66$; 6QC, 1.4 ± 0.4, $n = 65$. The data were acquired from three biological replicates.

only after incubation with both FAP and CATL in either order but not when individual proteases were used (Supplementary Fig. 12). We first tested the FAP-CAT probe in the 4T1 breast tumour model for direct comparison to 6QC and the single-substrate FAP probe GPS (the structure of the GPS probe is provided in Supplementary Fig. 11). Probe signal in splayed 4T1 tumours 4 h after injection (10 nmol, i.v.) confirmed an increase in fluorescence contrast for the FAP-CAT probe compared with the single-substrate probes 6QC and GPS (Fig. 6b; all of the splayed tumour images are provided in

Supplementary Fig. 13). The FAP-CAT probe also showed significantly increased overall signal and TBR within 4T1 tumours compared with both single-substrate probes (Fig. 6c,d). Interestingly, the signal arising from FAP-CAT in splayed tumours was more concentrated at the outer margins of the tumour compared with signal from activated DEATH-CAT-2, of which the most intense signal was found in the core of the tumour (vide infra). Immunofluorescence analysis of FAP expression in sectioned 4T1 tumours confirmed that the probe fluorescence is found at the edge of the tumour and

Fig. 8 | Evaluation of DEATH-CAT–FNIR in a mouse model of lung metastasis. a, Screen capture from a recorded video on the da Vinci surgical robot with the FireFly detector. Images show screen capture of fluorescence (left) and bright-field (right) images of lungs bearing metastases 16 h after tail-vein injection of DEATH-CAT–FNIR (20 nmol). **b**, Screen capture of ex vivo left lung bearing metastases 16 h after injection of DEATH-CAT–FNIR (20 nmol). The white arrows indicate the same tumour nodules identified using all fluorescence detection modalities. **c**, Representative bright-field, rainbow plot and overlay images of the resected lungs from **a** and **b**. Scale bars, 3 mm. The images are representative of a total of four images. **d**, Rainbow plot images of unstained sections from the left lung from **b** (top) and H&E-stained adjacent sections (bottom; with inlays for tumour regions). Magnification (×10) of metastases identified in fluorescence scans (indicated by the black boxes) are shown. The images are representative of five sections obtained in a stepwise manner through each tissue. Scale bars, 1 mm (middle row), 100 µm (bottom row). For **c** and **d**, fluorescence intensity scales are arbitrary RFU. For **a**–**d**, the arrow heads indicate the location of the metastases identified in all imaging modalities.

localizes with FAP expression (Fig. 6e). In the core of the tumour, FAP expression and probe activation are low, consistent with previous reports that FAP activity is localized at the invasive edges of tumours[41–43] (Supplementary Fig. 14).

Detecting lung cancer metastases using AND-gate probes. To demonstrate the ability of the probes to detect small metastatic cancer lesions, we further evaluated the AND-gate probes in a metastatic lung cancer model. Mice were injected with metastatic $Kras^{G12D/+}Tp53^{-/-}$ lung adenocarcinoma cells (1×10^5 cells, i.v.), which resulted in seeding and growth of cancer lesions in the lungs[44,45]. Three weeks after seeding of cancer cells, mice were injected with DEATH-CAT-2 and FAP-CAT as well as the single-substrate probes 6QC and GPS (30 nmol, i.v.). Mice were euthanized and resected lungs were imaged 16 h after injection (Fig. 7a). Both AND-gate probes were able to detect lung metastases, including those that were less than 1 mm in diameter. The imaged mouse lungs were sectioned, stained with H&E and evaluated for the presence of lung metastases. The location of fluorescent probe signals correspond to the location of metastases on the basis

of H&E staining (Fig. 7b). Furthermore, the DEATH-CAT-2 probe produced a significantly brighter signal compared with FAP-CAT and 6QC (Fig. 7c) and both AND-gate probes displayed better TBRs than 6QC when compared with surrounding tissue and lung tissues from healthy mice (Fig. 7d,e). The single-substrate FAP probe GPS was not able to clearly define lung metastases and was not evaluated further.

As DEATH-CAT-2 was the best performing AND-gate probe for detecting metastatic lung tumours, we assessed the ability of the DEATH-CAT–FNIR probe to be used for robotic surgery in this model. We therefore dissected mice bearing metastatic lung tumours 16 h after probe injection using the Da Vinci surgical system (Supplementary Video 2). Screen captures of the recorded dissection demonstrate that the NIR camera system enabled us to detect metastases in the lungs in real time (Fig. 8a,b). We then resected lungs and subsequently imaged the tissues using the LiCor Pearl imaging system (Fig. 8c). This analysis confirmed the probe selectivity for metastatic lesions and matched with the data obtained in real time using the Firefly detector. Finally, to demonstrate the ability of the AND-gate probe to be used as a diagnostic indicator as

well as a real-time optical contrast agent, we fixed and sectioned the resected lungs to confirm that fluorescent hot spots correspond to sites of tumours. Metastatic lesions were clearly visualized by fluorescence signal from the probe in scanned tissue sections and this signal matched the location of tumour cells as determined by adjacent H&E stained slides (Fig. 8d). The DEATH-CAT–FNIR probe was able to locate metastatic cancer lesions with a diameter of less than 1 mm using both the robotic surgical system and LiCor imaging system. Furthermore, the fluorescence signal from the probe was able to withstand tissue fixation conditions (4% paraformaldehyde), enabling sectioned tissues to be scanned for identification of metastatic lesions as a diagnostic aid.

Discussion

The sensitive and accurate detection of tumour margins and metastases is a central goal for effective treatment of any type of solid tumour during surgery. There are presently a number of effective ways to image the location of a tumour in the body. However, most of the current imaging strategies are not suitable for real-time applications during surgery. Furthermore, they often depend on contrast agents that lack the level of specificity needed to be used in diverse cancer tissue types. Recent efforts to address these limitations in current imaging technologies have focused on targeted contrast agents that produce fluorescence signals only within the tumour microenvironment. Although this approach has proven to be valuable and several agents are currently in human clinical trials, there remains a need to find strategies to improve the selectivity of optical contrast agents so that they can be used in almost any type of tumour resection. We and others have developed activatable 'smart probes' that turn on a fluorescence signal when processed by a protease that is highly activated in tumour tissues. These reagents provide overall high contrast in some tumour types in which the level of the active protease in the surrounding normal tissues is low. Here we describe a general strategy to generate the next-generation of optical smart probes that require processing by multiple tumour-associated enzymes. This multivariate AND-gate sensor has the potential for highly increased tumour selectivity by incorporating substrates that are specifically processed by enzymes that exist in normal tissues but that are found together only in the tumour microenvironment. Using this strategy, background signal in healthy surrounding tissue is eliminated, resulting in high image contrast and clear margin detection, even for probes with overall low signal strength.

We chose to build the first AND-gate probe using two substrates that are cleaved by cysteine cathepsins[20,25] and Casp3 (refs. [46,47]). We chose this combination of enzymes owing to their non-overlapping primary sequence specificity. Furthermore, although all tissues contain some level of active cathepsins, Casp3 is activated only during the late stages of apoptosis, which typically does not take place in healthy tissues. Multiple types of cell death are activated within tumours as the result of several factors, including nutrient and oxygen starvation[32,48,49]. Dying cells within the tumour activate infiltrating immune cells, such as macrophages that then clear the cells by lysosomal engulfment. Thus, a specific niche exists within the tumour microenvironment in which both lysosomal and apoptotic proteases coexist, making these proteases ideal choices for use in tumour-specific AND-gate sensors.

To show the generality of the AND-gate approach, we combined the general cathepsin substrate with FAP. The FAP protease is another ideal target for an AND-gate probe because it has increased activity in numerous cancer types and is generally not active in normal tissues[36,37,42]. Furthermore, FAP has a unique substrate specificity profile preferring a P1 Pro, which is orthogonal to many other protease sequence preferences[38]. This probe combined two sequences specific for an extracellular protease and lysosomal proteases, which could accumulate within tumours. By contrast, the single-substrate probe that targeted only FAP did not accumulate

in tumours to the same extent. This suggests that combining a lysosomal protease with an extracellular protease sequence can be a means of achieving activation and accumulation within a tumour for more specific visualization of tumour margins and metastases.

As we have designed a general strategy in which the fluorescent reporter is attached to a central linker that is the final end product of probe processing, it is possible to further engineer our first-generation AND-gate probes to respond to additional enzymatic processes beyond a binary set of targets. This hub-and-spoke model should also be amenable to further optimization of chemistry to enable the production of a diverse range of AND-gate sensors by swapping the spokes around the central fluorescent hub. Furthermore, it is possible to replace the current quencher–fluorophore strategy with a Förster resonance energy transfer (FRET) fluorophore pair that would enable ratiometric imaging to detect probe distribution as well as activation. This strategy would help to reduce the heterogeneity of imaging signals due to differential probe distribution while also reducing background signals by enabling quantification on the basis of a ratio of signals, which can be a large value even when probe concentrations are low. At present, we are working to develop ratiometric AND-gate probes as well as multivariate versions that respond to more than two proteases. There are many additional proteases that have been shown to be preferentially activated in solid tumours of diverse origins, and many of these proteases have defined substrate specificity that would render the design of next-generation AND-gate sensors straightforward.

In addition to using the multivariate AND-gate strategy to improve imaging contrast, it should also be possible in theory to apply this approach to selective drug delivery applications. Such a strategy would require the attachment of an individual or multiple drugs to the central hub through linkages that block activity of the agents and that can be processed within a specific tissue location. We envisage such an AND-gate therapy that releases one or more active drugs only when multiple proteases cleave the linkages that tether the molecules to one another. We are presently exploring approaches to use the AND-gate approach for such applications.

Here we show that the DEATH-CAT–FNIR probe is compatible with existing robotic surgical systems and workflows to enable visualization of residual tumour tissue that remains after removal of a primary mass and small metastases (<1 mm in diameter). These results suggest that the AND-gate strategy will enhance the effectiveness of tumour resections during fluorescence-guided surgery, even in locations in which high background signal would normally limit effective visualization of the margin.

Outlook

Overall, the studies presented here provide a roadmap for designing optical contrast agents that respond to unique enzymatic signatures that are indicative of a disease state. In the current design, we demonstrate the utility of the AND-gate approach using substrates that are uniquely processed by two proteases, which are both activated in the tumour microenvironment. The design of the AND-gate protease probe used here required engineering of the linker group to prevent activation by undesired protease activities found in normal healthy tissues and, ultimately, resulted in contrast agents that both improve tumour selectivity and also increase tumour uptake resulting in a brighter overall signal. At present, we are working to further optimize the central linker such that higher-order probes can be rapidly generated by attachment of various substrates containing quenchers using orthogonal chemistry. This should enable the synthesis of probes with high selectivity for a diverse range of cancer types based on proteolytic signatures of those tumours. It should also, in principle, enable the generation of probes that respond to other classes of enzymes in diverse disease states that are capable of processing substrates to liberate a central fluorescent or therapeutic fragment.

Methods

Chemistry methods. The synthesis protocols are provided in the Supplementary Information.

Biology methods. *General cell culture.* 4T1 cells and RAW246.7 macrophages were cultured separately as previously described[20,50]. RAW246.7 macrophages were cultured in Dulbecco's modified Eagle's medium (DMEM, Gibco, 11965-092) containing $4.5\,g\,l^{-1}$ of glucose supplemented with 10% fetal bovine serum (FBS, GeminiBio, 100602), and $100\,U\,ml^{-1}$ penicillin and $100\,\mu g\,ml^{-1}$ streptomycin (Gibco, 15140-122). 4T1 cells were cultured in Roswell Park Memorial Institute (RPMI, Corning, 10-040-CV) 1640 medium containing $2\,g\,l^{-1}$ of glucose, $0.3\,g\,ml^{-1}$ of L-glutamine, and supplemented with 10% FBS and $100\,U\,ml^{-1}$ penicillin and $100\,\mu g\,ml^{-1}$ streptomycin. The $Kras^{G12D/+}Tp53^{-/-}$ lung adenocarcinoma cells were cultured in DMEM containing $4.5\,g\,l^{-1}$ of glucose supplemented with 10% fetal bovine serum (FBS) and $100\,U\,ml^{-1}$ penicillin and $100\,\mu g\,ml^{-1}$ streptomycin.

Fluorogenic substrate assay. All proteases were active-site titrated as previously described to obtain active protease concentrations[20]. The buffers used for caspases, fibroblast activation protein-α and cathepsins were made as previously described[20,33]. The reducing agent 1,4-dithiothreitol (DTT, VWR, 0281) was freshly added to buffers immediately before use. All assays were conducted in black, opaque flat-bottom 384-well plates (Greiner Bio-One, 781076). For single-substrate probes and the first cleavage of AND-gate probes, compounds were diluted in the respective protease buffer from 10 mM stock solutions in DMSO (Santa Cruz Biotechnology, sc358801), and 15 μl of substrate (20 μM) was added to each well. Immediately before beginning fluorescence measurements, 15 μl of protease was added to wells containing substrate using a multichannel pipette. All proteases were at a final concentration of 10 nM in the well unless otherwise indicated. Fluorescence measurements for probes containing a sulfo-Cy5 were read above the well with a Biotek Cytation3 Imaging Reader (7.00 mm read height; gain = 100; ex/em, 640/670 nm; normal read speed). Fluorescence measurements for probes containing ICG or FNIR tag fluorophores were read above the well with a SpectraM2 plate reader (7.00 mm read height; for ICG: ex/em, 780/820 nm; for FNIR tag: ex/em, 765/790 nm; normal read speed).

After confirming that AND-gate probes are not activated after a single addition of protease, probes were incubated with single proteases in an Eppendorf tube before the second protease addition and fluorescence measurements. AND-gate probes or negative controls (40 μM) were initially digested in 20 nM protease in the respective protease buffer. After 2 h at 37 °C, reactions with cathepsin buffer (pH 5.5) were exhausted by adding 2 M NaOH (1.4 μl per 100 μl of buffer) and were then diluted with caspase buffer to obtain a concentration of 20 μM total substrate (pH 7.0). Reactions containing caspase buffer (pH 7.0) were exhausted by adding 1 M HCl (2 μl per 100 μl of buffer) and were then diluted with cathepsin buffer to obtain a final concentration of 20 μM total substrate (pH 5.5). The singularly processed probes were added to wells (15 μl) and the second protease was added immediately before beginning fluorescence measurements (15 μl, 10 nM final protease concentration, 10 μM final substrate concentration). Fluorescence signal over time was measured as described above.

Live-cell fluorescence microscopy assay. RAW246.7 macrophages and 4T1 cells were diluted to 1×10^5 cells per ml with their respective medium and then mixed at a 1:1 ratio. The mixture of cells was seeded in a 96-well half-area μClear-bottom cell culture plate (Greiner Bio-One, 675096) at 30 μl per well, and the cells were allowed to adhere to the bottom of the plate for 24 h. Next, cells were incubated with DMSO (1%, v/v) or etoposide (5 μM). After 24 h incubation with DMSO or etoposide (Sigma-Aldrich, E1383), probes were added to the cell medium (5 μl, 1 μM) and incubated for 2 h. Hoechst 33342 (Invitrogen, H3570) was then added to the medium ($5\,\mu g\,ml^{-1}$) and the cells were imaged using a ×40 oil-emersion objective on a Zeiss Axiovert 200M confocal microscope. Acquired Z stacks consisted of 24 16-bit images taken in 1 μm increments apart beginning and ending 12 μm from the focal plane. The channels used were set on separate tracks. The channel settings were as follows. Cy5: gain = 545, laser ex = 639 nm, 2% power; Hoechst 33342: gain = 750, laser ex = 405 nm, 4% power, and differential interference contrast (DIC), T-PMT from Cy5 channel, gain = 480.

Images were processed using ImageJ v.1.52p[51]. Zeiss image files (.csi) were opened using the Bio-Formats plug-in. Images shown are flattened from Z stacks by taking the maximum intensity in each pixel using the Z projection function. All of the images were adjusted to the same contrast and brightness levels. The corrected total cellular fluorescence (CTCF) was determined by manually tracing cells using the region of interest manager function (ROI Manager) based on the DIC and nuclear staining images, and measuring the total fluorescence within each cell from the flattened Z-stack images. CTCF was calculated according to the following formula: CTCF = integrated density − (area of cell × average background). The average background was obtained by tracing circles where no cells were present and averaging the overall signal. Cells that were overlapping or on the edge of the image were not counted. CTCF measurements were normalized to the DEATH-CAT-2 DMSO-treated control to obtain fold-change values.

Animal models and fluorescence imaging. All of the experiments involving animals were approved and conducted in accordance with the current National Institutes of Health and Stanford University Institutional Animal Care and Use Committee guidelines. All of the animals were kept in a Stanford University Medical School housing facility in a climate-controlled room (23 °C, 40–60% humidity) under a 12 h light–12 h dark cycle. All in vivo and ex vivo imaging was conducted using a LiCor Pearl Trilogy imaging system. The three excitation/filter sets used for imaging include the 700 nm, 800 nm and white-light channels (resolution, 85 μm or 175 μm; focus setting, zero). All of the displayed images were normalized across experimental cohorts and colour scales indicate relative arbitrary fluorescence units. Scanned unstained sections of tissue were imaged using a LiCor Odyssey CLx flatbed scanner (excitation/filter setting, 800 nM; resolution, 21 μm; quality, high). Live mice were imaged at indicated time points after i.v. tail-vein injection of probe under isoflurane anaesthesia (Fluriso, 13985-528-60). Anaesthesia was delivered into a nose cone or sealed chamber using a small animal isoflurane vaporizer (VetEquip, VE6780) with induction at 3% and maintenance at 2% isoflurane flow with oxygen as the carrier. All fluorescence signals were normalized using ImageStudioLite (LiCor, v.5.2). For quantitative analysis of fluorescence signal, signal within an ellipsoid ROI surrounding the tumour or metastases was used to calculate the average fluorescence pixel intensity. For TBR calculations, the average signal for each tumour or metastases was divided by the average signal of directly adjacent healthy tissue using the same size ROI.

For ex vivo analysis, mice were euthanized under isoflurane anaesthesia by cervical dislocation after in vivo imaging was completed. Average fluorescence intensity was measured in each organ by placing an ellipsoid ROI encompassing the organ and normalizing each average intensity to the average fluorescence intensity in the tumours.

4T1 breast tumour model. 4T1 cells suspended in 1× phosphate-buffered saline (PBS, 100 μl, 1×10^6 cells per ml) were injected subcutaneously into the third and eighth mammary fat pads of BALB/c ByJ female mice (aged 6–8 weeks; Jackson Laboratory). Mice were monitored for tumour formation and were injected with probe for imaging between 7–10 d after seeding 4T1 cells. Probes were dissolved in 1× PBS (10% DMSO) and injected i.v. in the tail vein (100 μl, 10 nmol or 20 nmol) using a 1 ml insulin syringe (BD biosciences, 28 gauge). Hair was removed to expose the tumours using Nair lotion while the mice were under anaesthesia 1 h before imaging.

Histological analysis of 4T1 tumour sections using confocal fluorescence microscopy. 4T1 breast tumours in the mammary fat pads of BALB/c mice injected with probe were excised post mortem. The tumour tissues were fixed in neutral buffered formalin solution (4% formaldehyde, Sigma-Aldrich, HT501128) for 24 h at 4 °C. The fixed tumour tissues were then soaked in 30% (w/v) sucrose (RPI, S24065) in 1× PBS for 24 h at 4 °C. Tumour samples were embedded in optimal cutting temperature compound (O.C.T., Tissue-Tek, 4583) and kept at −80 °C until further use. Embedded tissues were then cryosectioned (5–10 μm) onto glass slides. The samples were stored at −20 °C before staining. The cryosections were first washed three times with 1× PBS in a slide chamber. The samples were then blocked with 3% (w/v) BSA (Thermo Fisher Scientific, BP1600) for 24 h at 4 °C. Samples were washed 3× with 0.5% (w/v) BSA, then tissues were outlined with a hydrophobic pen, followed by incubation with 1:2,500 dilution of primary antibodies against CD68 (rat anti-mouse, Bio-Rad), cleaved Casp3 (rabbit anti-mouse, Cell Signaling) or FAP (rabbit anti-mouse, R&D Systems) in 0.5% (w/v) BSA in 1× PBS for 24 h at 4 °C. The samples were then washed five times with 0.5% (w/v) BSA in 1× PBS. Tissues were next incubated with anti-rat Alexa Fluor 488 and anti-rabbit Alexa Fluor 594 secondary antibodies (Invitrogen) diluted 1:5,000 for 1 h at room temperature. Tissues were washed five times with 0.5% (w/v) BSA in 1× PBS, followed by three washes with 1× PBS. Tissues were mounted with Vectashield mounting medium containing 4,6-diamidino-2-phenylindole (DAPI) (Novus Biologicals, H-1200-NB).

Sections of tumours were imaged using a ×40 oil-emersion objective on a Zeiss Axiovert 200M confocal microscope. Images are of a single focal plane (16 bit). All channels were set on separate tracks for imaging. The channel settings were as follows. Cy5: gain = 730, laser ex = 639 nm, 20% power; A594 (cleaved Casp3): gain = 600, laser ex = 555 nm, 4% power; A488 (CD68): gain = 640, laser ex = 488, 4% power; DAPI: gain = 600, laser ex = 405 nm, 2% power. Additional details about the primary and secondary antibodies used are provided in the Reporting Summary.

Lung metastases mouse model. Male B6129SF1/J mice (aged 8–10 weeks, Jackson Laboratory) were injected with 1×10^5 $Kras^{G12D/+}Tp53^{-/-}$ lung adenocarcinoma cells (i.v., tail vein, 200 μl) suspended in 1× PBS. Mice bearing lung metastases or healthy mice were injected with probes 21–23 d after initial cancer cell injections (i.v., tail vein, 100 μl). Probes were diluted in 30% (v/v) PEG 400 (Hampton Research, HR2–603), 10% (v/v) DMSO in 1× PBS. Mice were euthanized and their lungs were resected for imaging.

Robotic fluorescence-guided surgery. Breast tumour-bearing mice (4T1) or mice with lung metastases were administered with the indicated probes i.v. in the tail vein (100 μl, 20 nmol in 30% (v/v) PEG 400, 10% (v/v) DMSO in 1× PBS) 2 h

before surgery. Robotic fluorescence-guided surgery was performed using an FDA-approved da Vinci Xi surgical system equipped with a Firefly fluorescence detector. Surgery on breast-tumour-bearing mice was initially performed under inhaled isoflurane using the same vaporizer delivery system and method as described in the 'Animal models and fluorescence imaging' section. For presurgical pain relief, buprenorphine ($0.05\,mg\,kg^{-1}$) was administered i.p. while under inhaled anaesthesia. After resection of the tumours, mice were put into deep sedation with ketamine–xylazine solution ($80\,mg\,kg^{-1}$ ketamine, $10\,mg\,kg^{-1}$ xylazine, i.p.), followed by cervical dislocation. Mice bearing lung metastases were euthanized in the same manner before fluorescence-guided surgery to avoid undue pain during the exploratory dissection. Imaging after euthanasia and excision of the lungs was necessary because the fluorescence output is not observable below the peritoneum during live-animal imaging. Euthanizing the animal does not affect the fluorescence output of the probes. Breast cancers and lung metastases were detected using a combination of white light and fluorescence signal based on probe activation as a guide to determine tumour margins from healthy tissue. Videos of the surgical procedures are provided in the Supplementary Information.

Histopathological analysis of 4T1 tumours. Tissues including the bulk 4T1 breast tumour and tissue adjacent to the tumour were excised, fixed in 4% formaldehyde in buffered solution, processed routinely, sectioned at $5–10\,\mu m$ and stained with H&E. Adjacent subcutaneous and cutaneous tissues were embedded in paraffin with the subcutaneous side down (bulk tumour adjacent), such that each slide contained both probe-positive and probe-negative regions. Step-sections were taken through the entirety of the tissue at $100\,\mu m$ intervals.

Histopathological analysis of lung metastases. After robotic surgery and/or imaging, resected lungs bearing metastases were fixed in 4% formaldehyde in buffered solution for 24 h at 4 °C. Tissues were then soaked in 30% (w/v) sucrose in 1× PBS for 24 h. Lungs were embedded in O.C.T. compound and step-sectioned at $10\,\mu m$ through the tissue at $100–200\,\mu m$ increments. Sections were H&E stained and evaluated for the presence of lung metastases and correlated with fluorescence signals. For mice injected with DEATH-CAT–FNIR, unstained lung sections were imaged using a LiCor Odyssey CLx flatbed scanner and adjacent sections were stained with H&E for comparison.

Reporting Summary. Further information on research design is available in the Nature Research Reporting Summary linked to this article.

Data availability
The main data supporting the results in this study are available within the paper and its Supplementary Information. The raw and analysed datasets generated during the study are too large to be publicly shared, yet they are available for research purposes from the corresponding author on reasonable request.

References
1. Tringale, K. R., Pang, J. & Nguyen, Q. T. Image-guided surgery in cancer: a strategy to reduce incidence of positive surgical margins. *Wiley Interdiscip. Rev. Syst. Biol. Med.* **10**, e1412 (2018).
2. Orosco, R. K. et al. Positive surgical margins in the 10 most common solid cancers. *Sci. Rep.* **8**, 5686 (2018).
3. Yossepowitch, O. et al. Positive surgical margins after radical prostatectomy: a systematic review and contemporary update. *Eur. Urol.* **65**, 303–313 (2014).
4. Winter, J. M. et al. 1423 pancreaticoduodenectomies for pancreatic cancer: a single-institution experience. *J. Gastrointest. Surg.* **10**, 1199–1210 (2006).
5. McGirt, M. J. et al. Extent of surgical resection is independently associated with survival in patients with hemispheric infiltrating low-grade gliomas. *Neurosurgery* **63**, 700–707 (2008).
6. Brouwer de Koning, S. G., Vrancken Peeters, M., Jozwiak, K., Bhairosing, P. A. & Ruers, T. J. M. Tumor resection margin definitions in breast-conserving surgery: systematic review and meta-analysis of the current literature. *Clin. Breast Cancer* **18**, e595–e600 (2018).
7. Morrow, M. et al. Trends in reoperation after initial lumpectomy for breast cancer: addressing overtreatment in surgical management. *JAMA Oncol.* **3**, 1352–1357 (2017).
8. Weissleder, R. & Pittet, M. J. Imaging in the era of molecular oncology. *Nature* **452**, 580–589 (2008).
9. Valdes, P. A., Roberts, D. W., Lu, F. K. & Golby, A. Optical technologies for intraoperative neurosurgical guidance. *Neurosurg. Focus* **40**, E8 (2016).
10. Zhang, J. et al. Nondestructive tissue analysis for ex vivo and in vivo cancer diagnosis using a handheld mass spectrometry system. *Sci. Transl. Med.* **9**, eaan3968 (2017).
11. Thill, M. MarginProbe: intraoperative margin assessment during breast conserving surgery by using radiofrequency spectroscopy. *Expert Rev. Med. Devices* **10**, 301–315 (2013).
12. Garland, M., Yim, J. J. & Bogyo, M. A bright future for precision medicine: advances in fluorescent chemical probe design and their clinical application. *Cell Chem. Biol.* **23**, 122–136 (2016).
13. Gossedge, G., Vallance, A. & Jayne, D. Diverse applications for near infra-red intraoperative imaging. *Colorectal Dis.* **17**, 7–11 (2015).
14. Ferraro, N. et al. The role of 5-aminolevulinic acid in brain tumor surgery: a systematic review. *Neurosurg. Rev.* **39**, 545–555 (2016).
15. Nguyen, Q. T. & Tsien, R. Y. Fluorescence-guided surgery with live molecular navigation—a new cutting edge. *Nat. Rev. Cancer* **13**, 653–662 (2013).
16. Weissleder, R., Tung, C. H., Mahmood, U. & Bogdanov, A. Jr. In vivo imaging of tumors with protease-activated near-infrared fluorescent probes. *Nat. Biotechnol.* **17**, 375–378 (1999).
17. Whitley, M. J. et al. A mouse-human phase 1 co-clinical trial of a protease-activated fluorescent probe for imaging cancer. *Sci. Transl. Med.* **8**, 320ra324 (2016).
18. Whitney, M. et al. Ratiometric activatable cell-penetrating peptides provide rapid in vivo readout of thrombin activation. *Angew. Chem. Int. Ed. Engl.* **52**, 325–330 (2013).
19. Sakabe, M. et al. Rational design of highly sensitive fluorescence probes for protease and glycosidase based on precisely controlled spirocyclization. *J. Am. Chem. Soc.* **135**, 409–414 (2013).
20. Ofori, L. O. et al. Design of protease activated optical contrast agents that exploit a latent lysosomotropic effect for use in fluorescence-guided surgery. *ACS Chem. Biol.* **10**, 1977–1988 (2015).
21. Egeblad, M. & Werb, Z. New functions for the matrix metalloproteinases in cancer progression. *Nat. Rev. Cancer* **2**, 161–174 (2002).
22. Parks, W. C., Wilson, C. L. & Lopez-Boado, Y. S. Matrix metalloproteinases as modulators of inflammation and innate immunity. *Nat. Rev. Immunol.* **4**, 617–629 (2004).
23. Mohamed, M. M. & Sloane, B. F. Cysteine cathepsins: multifunctional enzymes in cancer. *Nat. Rev. Cancer* **6**, 764–775 (2006).
24. Aggarwal, N. & Sloane, B. F. Cathepsin B: multiple roles in cancer. *Proteom. Clin. Appl.* **8**, 427–437 (2014).
25. Yim, J. J., Tholen, M., Klaassen, A., Sorger, J. & Bogyo, M. Optimization of a protease activated probe for optical surgical navigation. *Mol. Pharm.* **15**, 750–758 (2018).
26. Erbas-Cakmak, S. et al. Molecular logic gates: the past, present and future. *Chem. Soc. Rev.* **47**, 2228–2248 (2018).
27. Stennicke, H. R., Renatus, M., Meldal, M. & Salvesen, G. S. Internally quenched fluorescent peptide substrates disclose the subsite preferences of human caspases 1, 3, 6, 7 and 8. *Biochem J.* **350**, 563–568 (2000).
28. Blum, G. et al. Dynamic imaging of protease activity with fluorescently quenched activity-based probes. *Nat. Chem. Biol.* **1**, 203–209 (2005).
29. Gajewski, T. F., Schreiber, H. & Fu, Y. X. Innate and adaptive immune cells in the tumor microenvironment. *Nat. Immunol.* **14**, 1014–1022 (2013).
30. Loser, R. & Pietzsch, J. Cysteine cathepsins: their role in tumor progression and recent trends in the development of imaging probes. *Front. Chem.* **3**, 37 (2015).
31. Olson, O. C. & Joyce, J. A. Cysteine cathepsin proteases: regulators of cancer progression and therapeutic response. *Nat. Rev. Cancer* **15**, 712–729 (2015).
32. Nikoletopoulou, V., Markaki, M., Palikaras, K. & Tavernarakis, N. Crosstalk between apoptosis, necrosis and autophagy. *Biochim. Biophys. Acta* **1833**, 3448–3459 (2013).
33. Edgington-Mitchell, L. E. & Bogyo, M. Detection of active caspases during apoptosis using fluorescent activity-based probes. *Methods Mol. Biol.* **1419**, 27–39 (2016).
34. Ye, D. et al. Bioorthogonal cyclization-mediated in situ self-assembly of small-molecule probes for imaging caspase activity in vivo. *Nat. Chem.* **6**, 519–526 (2014).
35. Luciano, M. P. et al. A nonaggregating heptamethine cyanine for building brighter labeled biomolecules. *ACS Chem. Biol.* **14**, 934–940 (2019).
36. Busek, P., Mateu, R., Zubal, M., Kotackova, L. & Sedo, A. Targeting fibroblast activation protein in cancer—prospects and caveats. *Front. Biosci.* **23**, 1933–1968 (2018).
37. Pure, E. & Blomberg, R. Pro-tumorigenic roles of fibroblast activation protein in cancer: back to the basics. *Oncogene* **37**, 4343–4357 (2018).
38. Edosada, C. Y. et al. Peptide substrate profiling defines fibroblast activation protein as an endopeptidase of strict Gly_2-Pro_1-cleaving specificity. *FEBS Lett.* **580**, 1581–1586 (2006).
39. Bainbridge, T. W. et al. Selective homogeneous assay for circulating endopeptidase fibroblast activation protein (FAP). *Sci. Rep.* **7**, 12524 (2017).
40. Zhang, H. E. et al. Identification of novel natural substrates of fibroblast activation protein-alpha by differential degradomics and proteomics. *Mol. Cell. Proteom.* **18**, 65–85 (2019).

41. Hua, X., Yu, L., Huang, X., Liao, Z. & Xian, Q. Expression and role of fibroblast activation protein-alpha in microinvasive breast carcinoma. *Diagn. Pathol.* **6**, 111 (2011).

42. Zi, F. et al. Fibroblast activation protein alpha in tumor microenvironment: recent progression and implications (Review). *Mol. Med. Rep.* **11**, 3203–3211 (2015).

43. Fang, J. et al. A potent immunotoxin targeting fibroblast activation protein for treatment of breast cancer in mice. *Int. J. Cancer* **138**, 1013–1023 (2016).

44. Winslow, M. M. et al. Suppression of lung adenocarcinoma progression by Nkx2-1. *Nature* **473**, 101–104 (2011).

45. DuPage, M. et al. Endogenous T cell responses to antigens expressed in lung adenocarcinomas delay malignant tumor progression. *Cancer Cell* **19**, 72–85 (2011).

46. Vickers, C. J., Gonzalez-Paez, G. E. & Wolan, D. W. Discovery of a highly selective caspase-3 substrate for imaging live cells. *ACS Chem. Biol.* **9**, 2199–2203 (2014).

47. Julien, O. et al. Quantitative MS-based enzymology of caspases reveals distinct protein substrate specificities, hierarchies, and cellular roles. *Proc. Natl Acad. Sci. USA* **113**, E2001–E2010 (2016).

48. Jaattela, M. Multiple cell death pathways as regulators of tumour initiation and progression. *Oncogene* **23**, 2746–2756 (2004).

49. Labi, V. & Erlacher, M. How cell death shapes cancer. *Cell Death Dis.* **6**, e1675 (2015).

50. Verdoes, M. et al. Improved quenched fluorescent probe for imaging of cysteine cathepsin activity. *J. Am. Chem. Soc.* **135**, 14726–14730 (2013).

51. Rasband, W. S. ImageJ (US National Institutes of Health, 1997–2011); http://imagej.nih.gov.stanford.idm.oclc.org/ij/

Acknowledgements

Author contributions

M.B. and J.C.W. conceived the AND-gate probe concept and designed all of the experiments. J.C.W. synthesized all of the AND-gate probes, conducted the fluorogenic substrate assays, live- and fixed-cell fluorescence microscopy experiments, and mouse model experiments. J.C.W. and M.B. wrote the text of the paper and constructed the figures with input from J.J.Y. and K.M.C.; M.T and J.J.Y. helped to perform live and ex vivo imaging during the 4T1 cancer mouse model experiment, including dissection of the mice. S.R. assisted with experimental design of the cancer mouse model studies. M.T. helped with the immunohistochemical analysis of 4T1 tumours. A.A., A.K. and J.S. assisted with the robotic surgery. K.M.C. evaluated H&E sections for the lung metastasis and 4T1 breast cancer mouse models.

Competing interests

J.S., A.K. and A.A. are employees of and shareholders of Intuitive Surgical Inc., which makes the da Vinci robotic surgical system used in this study. M.B. has received funding from Intuitive Surgical Inc. for work unrelated to the studies presented in this manuscript and does not hold stock or any advisory/consulting position with the company.

Additional information

Supplementary information is available for this paper at https://doi.org/10.1038/s41551-020-00616-6.

Correspondence and requests for materials should be addressed to M.B.

Reprints and permissions information is available at www.nature.com/reprints.

Publisher's note Springer Nature remains neutral with regard to jurisdictional claims in published maps and institutional affiliations.

nature research

Corresponding author(s): Matthew Bogyo

Last updated by author(s): Jul 31, 2020

Reporting Summary

Nature Research wishes to improve the reproducibility of the work that we publish. This form provides structure for consistency and transparency in reporting. For further information on Nature Research policies, see Authors & Referees and the Editorial Policy Checklist.

Statistics

For all statistical analyses, confirm that the following items are present in the figure legend, table legend, main text, or Methods section.

n/a	Confirmed	
☐	☒	The exact sample size (*n*) for each experimental group/condition, given as a discrete number and unit of measurement
☐	☒	A statement on whether measurements were taken from distinct samples or whether the same sample was measured repeatedly
☐	☒	The statistical test(s) used AND whether they are one- or two-sided *Only common tests should be described solely by name; describe more complex techniques in the Methods section.*
☐	☒	A description of all covariates tested
☐	☒	A description of any assumptions or corrections, such as tests of normality and adjustment for multiple comparisons
☐	☒	A full description of the statistical parameters including central tendency (e.g. means) or other basic estimates (e.g. regression coefficient) AND variation (e.g. standard deviation) or associated estimates of uncertainty (e.g. confidence intervals)
☐	☒	For null hypothesis testing, the test statistic (e.g. *F*, *t*, *r*) with confidence intervals, effect sizes, degrees of freedom and *P* value noted *Give P values as exact values whenever suitable.*
☒	☐	For Bayesian analysis, information on the choice of priors and Markov chain Monte Carlo settings
☒	☐	For hierarchical and complex designs, identification of the appropriate level for tests and full reporting of outcomes
☒	☐	Estimates of effect sizes (e.g. Cohen's *d*, Pearson's *r*), indicating how they were calculated

Our web collection on statistics for biologists contains articles on many of the points above.

Software and code

Policy information about availability of computer code

Data collection	All fluorescent measurements of mouse tumors in vivo and of ex vivo tumors and organs were taken using a LiCor Pearl Trilogy Imaging system with Image Studio Live Software (Ver 5.2). Live-cell fluorescent-microscopy images were taken using a Zeiss Axiovert 200 M confocal microscope under control of the Zeiss imaging software Zen (V 8.1.5.484). Plate-reader assays were measured using a Biotek Cytation3 Imaging Reader with the Gen5 microplate reader and imaging software (V 3.05.11), or a SpectraM2 plate reader and SoftMax Pro 7 software (V 7.0.3). Analysis of purity was conducted using a Thermo Fisher Finnigan Surveyor Plus under control of XCalibur software (v4.0). High-resolution mass spectrometry was completed on a Thermo Fisher Fusion under control of XCalibur (v4.2) software. Video of fluorescence-guided surgery was recorded using a da Vinci Xi Surgical System equipped with a Firefly fluorescence detector (proprietary software, no version available).
Data analysis	Data and statistical analyses were performed using Graphpad Prism (V 5.1). Image processing and analysis were done using ImageJ (v1.52p).

For manuscripts utilizing custom algorithms or software that are central to the research but not yet described in published literature, software must be made available to editors/reviewers. We strongly encourage code deposition in a community repository (e.g. GitHub). See the Nature Research guidelines for submitting code & software for further information.

Data

Policy information about availability of data

All manuscripts must include a data availability statement. This statement should provide the following information, where applicable:

- Accession codes, unique identifiers, or web links for publicly available datasets
- A list of figures that have associated raw data
- A description of any restrictions on data availability

The main data supporting the results in this study are available within the paper and its Supplementary Information. The raw and analysed datasets generated during the study are too large to be publicly shared, yet they are available for research purposes from the corresponding authors on reasonable request.

Field-specific reporting

Please select the one below that is the best fit for your research. If you are not sure, read the appropriate sections before making your selection.

☒ Life sciences ☐ Behavioural & social sciences ☐ Ecological, evolutionary & environmental sciences

For a reference copy of the document with all sections, see nature.com/documents/nr-reporting-summary-flat.pdf

Life sciences study design

All studies must disclose on these points even when the disclosure is negative.

Sample size	Target sample size was determined by previous experience with the methods used in this study, including fluorogenic substrate assays, small-animal imaging and immunofluorescence analysis. For the in vivo and ex vivo imaging studies, four or more mice were sufficient to identify differences in activatable-probe performance. For live-cell fluorescence-microscopy experiments, the number of cells counted was determined by the number of adherent cells within the fields of view for each sample that followed the criteria, including cells not on the edge of the field of view or overlapping with other cells. For immunofluorescence microscopy, sample size was determined by the number of tumors available for sectioning on the basis of the sample size of the small-animal imaging experiments.
Data exclusions	No data were excluded from analysis.
Replication	All experimental measurements were done for at least three biological replicates.
Randomization	All mice were randomly selected from cages into experimental groups. Individual tumor size, location, infiltrated immune cell status and any other factors that could impact the outcome of the study were not known prior to the injection of the probes and throughout the experimental workflow. Cells were randomly pipetted into wells prior to any live-cell microscopy experiments at equivalent cell densities.
Blinding	No formal blinding was used. The experiments conducted in this study are inherently blinded to the investigators until the completion of the experiment followed by data analysis because normalization procedures are necessary for comparison of cohorts.

Reporting for specific materials, systems and methods

We require information from authors about some types of materials, experimental systems and methods used in many studies. Here, indicate whether each material, system or method listed is relevant to your study. If you are not sure if a list item applies to your research, read the appropriate section before selecting a response.

Materials & experimental systems

n/a	Involved in the study
☐	☒ Antibodies
☐	☒ Eukaryotic cell lines
☒	☐ Palaeontology
☐	☒ Animals and other organisms
☒	☐ Human research participants
☒	☐ Clinical data

Methods

n/a	Involved in the study
☒	☐ ChIP-seq
☒	☐ Flow cytometry
☒	☐ MRI-based neuroimaging

Antibodies

Antibodies used	Lists of all primary and secondary antibodies used for immunofluorescence staining in this manuscript, including information about company, catalog number, lot number if available, clone number if available, and dilution: CD68: Rat anti-mouse, BioRad, Formly ABD SeroTec, Cat#: MCA1957, Clone: FA-11, Lot#: 260318, vendor validation: C, F, IF, IP, P, WB, dilution: 1:2,500 FAP-alpha: Rabbit anti-mouse, R&D systems, Cat#: ab53066, Lot#: GR3189477-28, vendor validation: WB, IHC-P, ELISA, IHC-Fr, ICC/IF, dilution: 1:2,500 Cleaved Casp3: Polyclonal Rabbit anti-mouse, Cell Signaling,Cat#: #9661S, Lot#: 37, vendor validation: WB, IP, IHC, IF, F, dilution: 1:2,500 anti-rat alexafluor488: Invitrogen, Cat#: A-11006, Lot#: 37977A, vendor validation: FC, ICC, IF, IHC, WB, dilution: 1:5,000 anti-rabbit alexafluor594: Invitrogen, Cat#: A-11012, Lot#: 99C2-2, vendor validation: FC, ICC, IF, IHC, WB, dilution: 1:5,000
Validation	Each antibody was validated through information in previous studies. References and/or links for each Ab are provided below. The antibodies were further validated experimentally via comparison to unstained controls. CD68: Devey, L. et al., Mol Ther. 2009, 17, 65.; Masaki, T. et al., Nepthrol. Dial. Transplant, 2003, 18, 178. FAP-alpha: Hellevik T. et al., Radiat Oncol. 2012, 13, 7(1):59. Cleaved Casp3: Hasko, J., et al., Acta Neuropathologica Communications, 2019, 7, 133. (> 250 publications on vendor website:

Eukaryotic cell lines

Policy information about cell lines

Cell line source(s)	RAW246.7 macrophages and 4T1 are from ATCC. The adenocarcinoma krasG12D/p53–/– cell line was obtained from the Winslow Lab at Stanford University. Relevant citations: Winslow, M.M. et al. Suppression of lung adenocarcinoma progression by Nkx2-1. Nature 473, 101-104 (2011); DuPage, M. et al. Endogenous T cell responses to antigens expressed in lung adenocarcinomas delay malignant tumor progression. Cancer cell 19, 72-85 (2011).
Authentication	Cell lines were not authenticated by our laboratory because they were obtained from a commercial source that verifies cell lines prior to sale.
Mycoplasma contamination	Cell lines were not tested for mycoplasma contamination.
Commonly misidentified lines (See ICLAC register)	No commonly misidentified cell lines were used.

Animals and other organisms

Policy information about studies involving animals; ARRIVE guidelines recommended for reporting animal research

Laboratory animals	6–8-week old, 20–25 g, Balb C/ByJ female mice, and 8–10-week old, 20–25 g, male B6129SF1/J mice, both from the Jackson Laboratory.
Wild animals	The study did not involve wild animals.
Field-collected samples	The study did not involve samples collected from the field.
Ethics oversight	All experiments involving animal care and experimentation were approved and conducted in accordance with current guidelines from the National Institutes of Health and the Stanford University Institutional Animal Care and Use Committee.

Note that full information on the approval of the study protocol must also be provided in the manuscript.